ChemElectroChem

Review
doi.org/10.1002/celc.202400441

Chemistry Europe
European Chemical
Societies Publishing

www.chemelectrochem.org

Theoretical and Experimental Insights into Dendrite Growth in Lithium-Metal Electrode

Behnam Ghalami Choobar,[a] Hamid Hamed,[a, b] Saeed Yari,[a, b, c] and
Mohammadhosein Safari*[a, b, c]

A stable lithium-metal electrode can enable the shift from the Li-ion batteries to the next generation chemistries such as Li–S and Li–O_2 with significant gains in the energy density and sustainability. This transition, however, is hindered by the dendrite formation, high chemical reactivity, and volume changes of the Li electrode. Although recent advancements in computational and experimental research have deepened our understanding of these issues, the primary obstacles to the commercialization of the lithium-metal batteries (LMBs) still persist. To address these challenges, a synergistic approach that combines computational and experimental strategies shows great promise. In this regard, this paper reviews the current experimental and theoretical understanding of the lithium-metal electrodes in view of the initiation and growth mechanisms of the lithium dendrites and interface instability. Leveraging the strengths of both approaches can offer a holistic insight into the LMB performance and guide the development of innovative designs for electrolytes and electrodes that can enhance the stability and performance of the LMBs.

1. Introduction

There is a soaring demand for the sustainable battery technologies to electrify the transport sector.[1] The International Energy Agency (IEA) projects the sales of electric vehicles (EVs) to surpass 100 million by 2035 commensurate with a pathway to achieve a net-zero CO_2 emission by 2050.[2] The state-of-the-art commercial lithium-ion batteries (LIBs) rely on a rocking-chair concept[3] where two Li-insertion active-materials at the cathode and anode host and exchange the cyclable lithium via a non-aqueous liquid electrolyte.[4] This battery concept has commercially matured over the last 3 decades offering an energy density of ~300 Wh/kg compared to ~150 Wh/kg at nineties when LIBs were first commercialized by Sony.[5] However, the need for more energy-dense alternative batteries has motivated old ongoing research to revive the forerunner Li-metal batteries (LMBs). This quest is simply incentivized by the low density (0.534 g/cm^3) and high electro-positivity (-3.04 V vs. standard hydrogen electrode) of the Li metal compared to the conventional insertion anodes such as graphite used in LIBs.[6–8] Moreover, the Li metal enables a radical shift from the transition-metal-oxides (TMO) cathodes such as $LiNi_xMn_yCo_{1-x-y}O_2$ (NMC) towards higher energy density alternatives like S and O_2 in Li–S and Li–O_2 batteries, respectively.[9,10] For instance, replacing the graphite and liquid electrolyte in LIBs with Li and solid electrolyte, respectively, can potentially rise the energy density of a Li-TMO cell above 440 Wh/kg.[8] The gain will be even higher with Li–S and Li–O_2 cells with practical energy density values estimated to mount up above 600 Wh/kg and 900 Wh/kg, respectively (Figure 1).[9,10]

Notwithstanding the alluring promises of LMBs, their practical and commercial reality has been hampered by a variety of technical issues. Inasmuch as the focus of the present review paper is Li, the fast degradation of this electrode is liable for the commercial immaturity of the rechargeable LMBs.[7,11] Particularly, the dendrite formation, high reactivity, volume changes, and the formation of dead Li are the major obstacles that abstain the LMBs from delivering a safe and stable cycle performance.[11–13] It is noteworthy that the emergence and success of the LIBs is somehow indebted to the commercial failure of the LMBs in the eighties. The Li/TiS_2 and Li/MoS_2 introduced by Exxon in 1978 and MoLi Energy in 1987, respectively, were among a series of pioneering rechargeable LMBs who lasted shortly on the market due to the major safety concerns triggered by the Li electrode.[14–16] Since then Li is known as the holy grail of the LMBs and remains as an important research topic in the battery community.[8,11,17,18] These researches particularly target mitigation strategies for the growth of dendrite during Li plating which results in short-circuiting and thermal runaway of the cell.[17] Moreover, the instable interface of the Li leads to the electrolyte degradation and the formation of "dead Li".[19] Additionally, Li metal is highly reactive, complicating the manufacturing and preservation processes of LMBs.[11–13,20–22] However, remarkable milestones have been marked toward the commercial viability of LMBs during the last decade. These include the development of artificial SEI layers,[23,24] the molecular design of electrolyte constituents,[25–29] techniques for regenerating dead Li,[19] and

---

[a] B. G. Choobar, H. Hamed, S. Yari, M. Safari
Institute for Materials Research (IMO-imomec), UHasselt, Martelarenlaan 42, B-3500 Hasselt, Belgium
E-mail: momo.safari@uhasselt.be

[b] H. Hamed, S. Yari, M. Safari
Energyville, Thor Park 8320, B-3600 Genk, Belgium

[c] S. Yari, M. Safari
IMEC division IMOMEC, BE-3590 Diepenbeek, Belgium

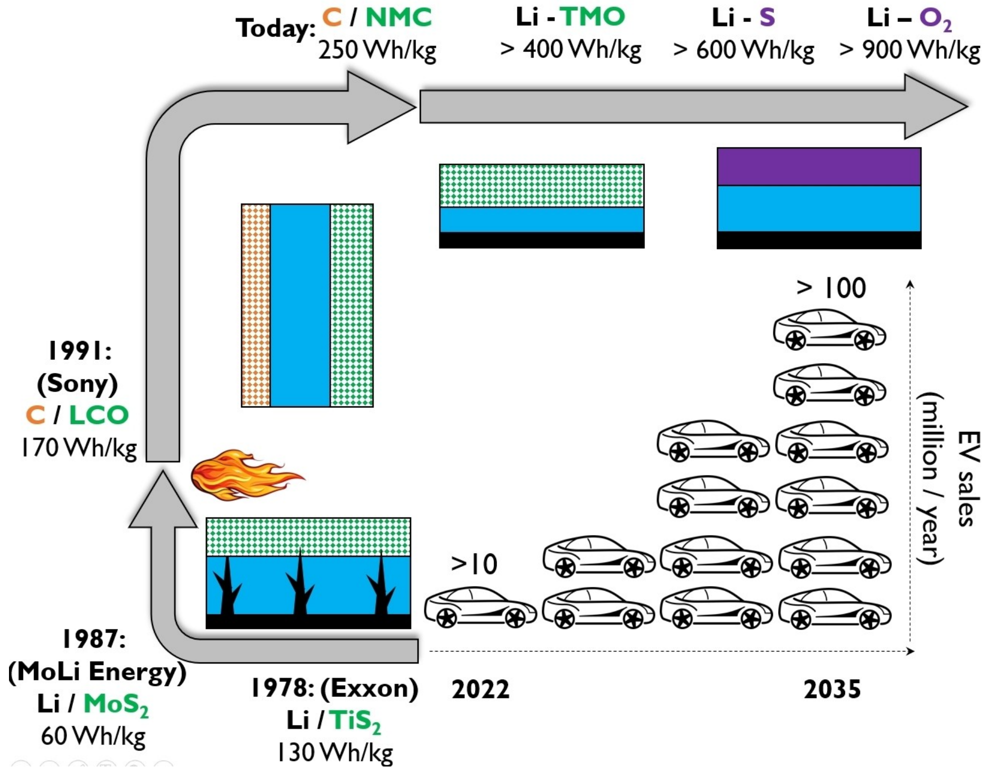

Figure 1. The shift of interest between the Li-metal and Li-ion batteries in view of time and the rising demand for battery-powered electric vehicles according to the net-zero-emission scenario.[2] The squared green and brown blocks represent the Li-insertion cathode materials and anode, respectively. The blue and black blocks are the electrolyte and Li metal, and the purple block stands for the next generation S and O_2 cathodes.

Behnam Ghalami Choobar received his Bachelor (2012) and Master (2014) degrees in Chemical Engineering from Sharif University of Technology (Iran). He obtained a PhD degree in Chemical Engineering from Amirkabir University of Technology (Iran, 2021), where he used multiscale simulation, namely quantum chemistry, molecular dynamics, and macroscopic simulation, to obtain deep insight into molecular interactions, and established a connection between molecular structure of electrolyte constituents and macroscopic performance of lithium-ion batteries. He joined the group of Electrochemical Engineering at Hasselt University in Feb 2022 as a postdoctoral researcher to work on the multi-scale modeling of advanced batteries.

Hamid Hamed earned his Bachelor and Master degrees in Chemical Engineering from Sharif University of Technology (Iran, 2016). He conducted his PhD in the group of Electrochemical Engineering at Hasselt University (2017–2022), focusing on the relationship between the mesoscale properties of the porous electrodes and the battery performance. Hamid is currently an FWO postdoctoral fellow at the group of Electrochemical Engineering at Hasselt University. His current research involves battery modeling, non-equilibrium thermodynamics, and multicomponent transport theory in porous media.

Saeed Yari earned his Bachelor of Science from University of Tabriz (Iran) and Master of Science from Tehran University (Iran) in Materials Engineering, specializing in Corrosion Engineering. He completed his PhD in 2022 at the group of Electrochemical Engineering at Hasselt University, where he investigated the inhomogeneities in porous electrodes and the resulting uneven aging processes. Currently, Saeed is an R&D Project Leader at the IMO-IMOMEC division of imec. His research interests encompass the design and engineering of porous electrodes and the use of in-situ characterization techniques for in-depth characterization of the performance and aging of batteries.

Mohammadhosein Safari received his bachelor degree from Tehran University (Iran, 2005) and Master and PhD degrees from Universite de Picardie Jules Verne (France, 2012). He spent his postdoctoral fellowship at University of Waterloo (Canada) before joining the Hasselt University at 2015 where he is currently a Professor and leads the group of Electrochemical Engineering. The research in his group centers around the coupling of experiment and modeling to understand and develop electrochemical systems for energy storage and conversion.

pressure-regulated deposition.[30,31] Additionally, advancements such as 3D anode structures,[32] protective coating,[33–35] electrolyte additives,[28,36] high concentration electrolytes (HCE)[37] and the innovative concept of localized HCE[38] are noteworthy.

This paper provides a short review of the major theoretical and experimental reports on the growth of Li dendrites in non-aqueous batteries. Particularly, the synergistic gain in combining the experimental and computational methods is highlighted. Section 2 provides a short summary of the experimental findings and the major characterization techniques employed to investigate the morphological instabilities of the Li electrode. Section 3 discusses the main physics-based modeling frameworks of the dendrite growth followed by the findings of the computational atomistic and molecular simulations in Section 4. Lastly, in Section 5, suggestions and guidelines for further research are proposed.

Experimental Insights into the Morphological Instability of Li Electrode

Our current understanding about the physical picture of the morphological instabilities at the Li electrode is based on the experimental insights gathered during the past three decades. The early observations of the arborescent like morphology of the Li deposits[39] and dendrite growth[40] through the polymer electrolytes and shorting the cell date back to nineties (Figure 2a). This physical picture has been refined with more subtle details about the initiation and growth mechanisms and their sensitivity to the electrolyte formulation and plating conditions,[39,41] thanks to the advanced characterization techniques of recent time (Figure 2b–k).[42]

To elucidate the underlying mechanisms of Li electrode behavior during electrochemical cycling, a suite of complementary experimental techniques has been employed. These encompass atomic force microscopy (AFM)[43] for real-time observation of surface dynamics and nanoscale morphology, cryo-electron microscopy (cryo-EM)[44] for high-resolution imaging of Li at the atomic level, optical microscopy for direct visualization of dendrite growth and evolution, and X-ray computed tomography (XCT)[45] for detailed 3D characterization of electrode structure. Synchrotron-based X-ray imaging further complements XCT by providing faster imaging speeds and higher resolution, crucial for capturing dynamic processes in operando.[42] Each method offers unique insights into the intricate processes occurring at the Li electrode interface, as summarized in Table 1.

Studies utilizing AFM have revealed the critical role of surface conditions in influencing dendrite growth. For instance, Kitta and Sano[46] observed that initial non-uniformities on the Li electrode surface can promote selective growth and lead to dendrite formation. Li et al.[47] have used peak force tunneling AFM to measure the surface roughness and electronic conductivity on a bare copper and a Cu3 N-modified copper. They showed that the nonuniform distribution of electronic current in the bare copper foil results in non-uniform plating and stripping, and thus Li dendrite formation (Figure 2e–h). The work of Wang et al.[48] using in-situ AFM demonstrated how current density significantly affects the nucleation and growth of Li. At low current densities, large, randomly dispersed nuclei form, while high current densities favor homogeneous nucleation with smaller particles. This has implications for dendrite morphology and overall electrode performance. The composition and concentration of the electrolyte play a pivotal

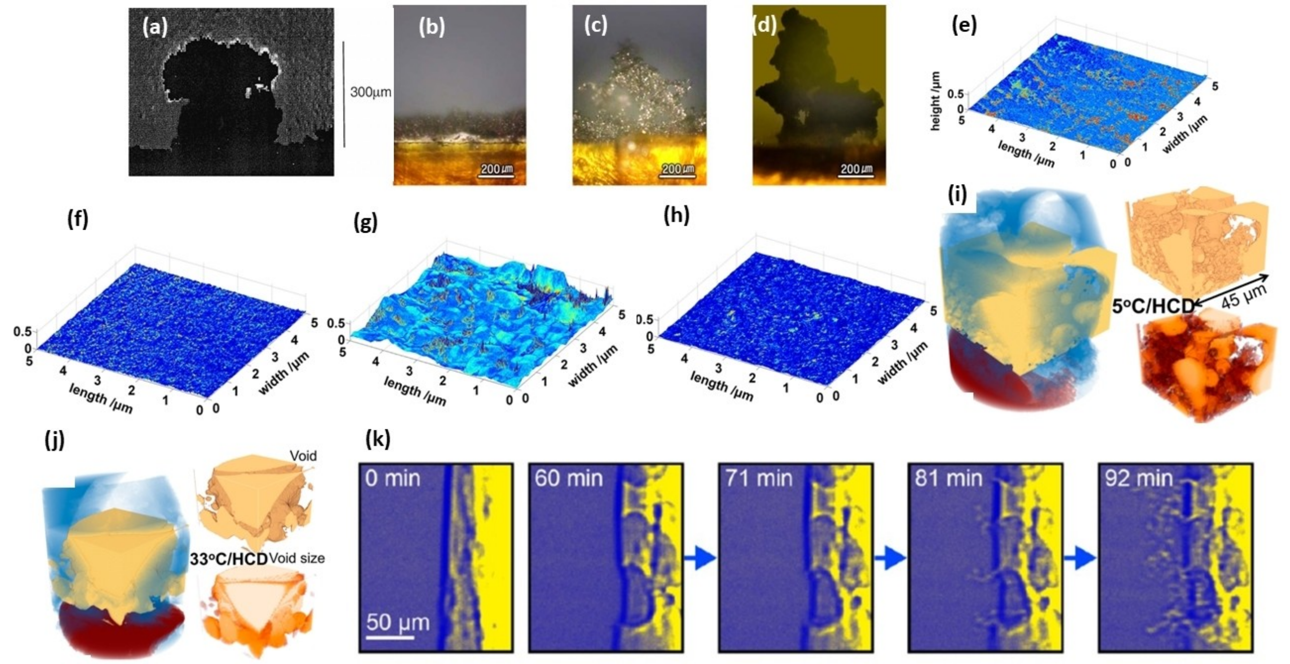

Figure 2. A growing dendrite in a symmetric Li/poly-ethylene-oxide-LiTFSI/Li cell at galvanostatic conditions (0.7 mA/cm^2),[39] Copyright 1999, Elsevier (**a**). The different density and morphology of the Li deposit after a plating throughput of 1.67 mAh/cm^2 with the three different electrolyte formulations of 1 M LITFSI in DME (**b**), 1 M LITFSI in tetraglyme (**c**), and 1 M LiI in tetraglyme (**d**),[41] Copyright 2014, Springer Nature. surface roughness measured by peak force tunneling AFM on bare and Cu_3N-modified Cu foil (**e**) and (**h**) at pristine state and (**g**) and (**i**) after the first Li plating and stripping processes[47] Copyright 2018, American Chemical Society. (**i**) and (**j**) internal void morphology analysis of Li deposit during plating extracted from the segmented sample from XCT results at different temperatures,[45] Copyright 2017, American Chemical Society. (**k**) formation of pits during Li stripping and the evolution of pits during the subsequent period of Li plating,[53] Copyright 2019, American Chemical Society.

Table 1. Comparison of experimental methods in the application of Li electrode characterization.[42–44]

Method	Theory	Strengths	Weaknesses	Applications	Efficiency
Atomic Force Microscopy (AFM)	Uses a sharp tip to scan the surface of a sample, measuring the interaction forces between the tip and the sample.	High-resolution imaging in-situ analysis ability to measure surface roughness and profile features at the nanoscale, nanoindentation capabilities ability to measure forces	limited to surface analysis can be time-consuming for large areas potential for tip-induced artifacts sensitivity to environmental factors like temperature and humidity	real-time observation of lithium deposition influence of surface film and initial conditions on dendrite growth impact of current density on nucleation and growth study of SEI formation and properties	High for surface analysis and real-time observation, lower for bulk characterization
Cryo-electron Microscopy (cryo-EM)	A beam of electrons is transmitted through a rapidly frozen sample to create a high-resolution image.	High-resolution imaging of lithium at the sub-angstrom level shields lithium from thermal damage caused by electron exposure slows down side reactions with atmospheric or water vapor enables the capture of high-resolution images of electron-sensitive lithium in its natural state	requires specialized equipment and expertise sample preparation can be challenging limited to very thin samples	Visualizing lithium dendrite growth direction understanding the impact of artificial protective layers on dendrite growth	High for visualizing nanoscale and atomic-scale structures, but lower for studying large-scale phenomena
Optical Microscopy	Uses visible light to magnify and observe the sample.	Relatively simple and inexpensive, can be used in-situ and operando provides real-time visualization of dendrite growth and morphology	Lower resolution compared to AFM and cryo-EM limited to surface observations difficult to quantify morphology changes	Real-time visualization of dendrite growth identifying growth mechanisms studying the impact of current density and electrolyte on morphology	Generally high for real-time observations, but lower for high-resolution imaging
X-ray Computed Tomography (XCT)	Uses X-rays to create cross-sectional images of a sample, which can be reconstructed into a 3D model.	High-resolution 3D imaging non-destructive can be used to study the internal structure of electrodes and batteries can differentiate between different materials using phase-contrast imaging or synchrotron-based X-rays	Expensive and requires specialized equipment limited to relatively small samples X-ray exposure can potentially damage some materials can be time-consuming for data acquisition and analysis	Studying lithium dendrite morphology morphological evolution during plating/stripping identifying different forms of lithium (needle-like, mossy-like, inactive) studying the impact of current density and temperature on morphology	High for 3D imaging and non-destructive analysis, but lower for real-time or dynamic studies
Synchrotron-based X-ray imaging	Uses synchrotron radiation to produce high-resolution images of the internal structure of materials.	Extremely high resolution Can penetrate deeper into materials compared to conventional X-rays Non-destructive Capable of capturing dynamic processes in real-time	Requires access to a synchrotron facility Expensive and complex setup Limited availability due to the need for specialized facilities	Detailed imaging of lithium electrode structures Studying the formation and growth of dendrites Investigating the impact of cycling conditions on elec-	High for detailed, non-destructive, and real-time imaging, particularly for studying dynamic processes

Table 1. continued

Method	Theory	Strengths	Weaknesses	Applications	Efficiency
				trode morphology Real-time tracking of structural changes during battery operation	

role in Li deposition and stripping. Wang et al.[49] have shown that lower salt concentrations resulted in improved coverage and a more even distribution of Li particles. Their findings revealed that at 0.2 M concentration, Li nucleation was prolonged, leading to an increased number of particles and a slower growth rate. Conversely, at 1 M concentration, Li particle growth accelerated, with particles merging quickly during deposition. In a study conducted by Stepein et al.,[50] researchers examined the effects of FEC additive on electrolytes. Their AFM results revealed that the presence of this additive led to a more uniform distribution of Li particles, resulting in a surface with enhanced smoothness. Liu et al.[51] highlighted the importance of balancing Li ion binding energy to the substrate, as excessive binding can hinder reversible stripping. Cryo-EM has provided valuable insights into the structure and morphology of deposited Li. Ju et al.[52] demonstrated that artificial protective layers can alter Li crystallization, promoting spherical growth over dendritic formations. Frisco et al.[45] used XCT and Zernike phase contrast to study the internal structure of lithium metal electrodes subjected to different current densities. They used 3D illustration of Li electrode to show that low current density resulted in uniform Li morphology, while high current density caused voltage spikes and potential electrolyte oxidation and copper dissolution. Temperature variations during cycling affected void size within the electrodes, with low temperatures causing smaller voids and higher temperatures leading to larger voids (Figure 2i and j). Yu et al.[53] utilized synchrotron-based X-ray imaging to provide comprehensive insights into the dynamics of Li plating and stripping in real-time, under conditions that closely mimic actual battery operations. This study sheds light on how various critical operating parameters influence the morphology of the Li deposits. These parameters include the concentration of lithium salts, current density, ionic strength, as well as the composition of the electrolytes and additives. Also, as shown in Figure 2k, they employed X-ray images to investigate pits formation during discharge. Wang et al.[24] revealed that electrochemically deposited lithium is primarily amorphous. Their cryo-TEM analysis highlights that while some crystalline LiF is present in the SEI, the amorphous nature of the electrochemically deposited Li plays a crucial role in its formation and properties, suggesting a more complex interaction within the SEI than previously thought. Fang et al.[54] employed cryo-EM to quantify "dead lithium," which is Li that becomes electrochemically inactive due to detachment from the current collector or encapsulation within the SEI. This inactive Li contributes to capacity loss and safety concerns in LMBs.

2. Macroscopic Physics-Based Models of DENDRITE Growth

2.1. Tip-Controlled Growth Mechanisms

The investigation into the electrodeposition of metals and dendrite growth spans a significant duration in scientific inquiry.[55] Before 1962, research in this field primarily provided qualitative observations regarding the factors influencing dendrite growth and their mechanisms.[55–57] Barton and Bockris[58] combined experiment and theory to investigate conditions that initiate and quantify parameters that control the growth rate if silver dendrites from an ionic molten salt on electrode substrates with different radii (50 to 500 μm). They reported two key experimental observations and proposed a model, accordingly, to formalize the growth rate of a dendrite: (I) the growth of dendrites initiates after a critical current density which directly and inversely scales with the concentration of the silver ions (C_0) and the radius of the electrode substrate, respectively, (II) at a given potential and concentration, although growth rates vary among dendrites, but are bounded by a consistent maximum velocity (ν_{max}). Their model links the growth rate of a dendrite by linking the overpotential (η), radius of the growing dendrite tip (r), assumed constant at a given overpotential, and the current density (i) on the plane normal to the axis of the growth.[58] In this model, three sources of overpotential are considered, namely the spherical diffusion (η_d), charge-transfer or activation (η_a), and the reversible potential deviation of a curved metal/electrolyte interface from that of a planar one (Δe_r):

$$\eta = \eta_a + \eta_d + \Delta e_r = \frac{i}{i_0}\frac{RT}{F} + \frac{irRT}{DC_0F^2} + \frac{2\gamma V}{Fr} \tag{1}$$

where Δe_r is expressed as a function of the surface tension between the metal and the electrolyte (γ), V is the molecular volume of silver, i_0 is the exchange current density, D is the diffusion coefficient, T is temperature, F is Faraday constant, and R is the universal gas constant. The dendrite growth rate (v) reads:

$$\nu = \frac{i}{F} \tag{2}$$

which is quadratic in r, according to Equation (1), enabling the determination of a maximum rate of dendrite growth:

$$\nu_{max} = \frac{DC_0F^2\eta^2}{2\gamma RT}\frac{\left[1-\frac{1}{1+\left[1+\frac{DC_0F^2}{2\gamma Vi_0}\eta\right]^{0.5}}\right]}{\left[1+\left[1+\frac{DC_0F^2}{2\gamma Vi_0}\eta\right]^{0.5}\right]}+\frac{1}{i_0} \tag{3}$$

According to Equation (3) for the dendrite growth velocity, for large values of i_0, i.e., pure diffusion and surface energy control mode, ν_{max} is proportional to η^2:

$$\nu_{max} = \frac{DC_0F^2}{8\gamma RT}\eta^2 \tag{4}$$

while at sufficiently low values of i_0, charge-transfer controlled, ν_{max} is proportional to η:

$$\nu_{max} = \frac{i_0V}{RT}\eta \tag{5}$$

According to Barton and Bockris' theoretical framework,[58] the preferential growth at the dendrite's tip is due to a faster spherical diffusion compared to a more sluggish diffusion at the base of the electrode.

Chazalviel[59] introduced the concept of space charge to explain and model the ramified electrodeposition of metals from a binary electrolyte. His theoretical analysis revealed that the dendrites should grow as fast as the drift velocity of the anions to minimize the thickness of the space-charge layer. He further interpreted the induction time, which is experimentally observed before start of the dendrite growth, as the time necessary to build the space charge by reaching a critical potential drop near the electrode (δV). This potential drop plays an important role in the Chazalviel's model and was linked to the ease of triggering microscopic instabilities at the electrode's surface. The theoretical findings of the Chazalviel was later confirmed by experiments in a series of papers co-authored by him, Brissot, and Rosso, using symmetric Li cells with polymer electrolytes[39,60] Particularly, the optical observation of the rate of dendrite growth was in line with the space-charge model in both low and high current regimes. It was shown that the experimental onset of the dendrite growth during galvanostatic plating correlates very well with the Sand's time (τ_s), time to deplete the ions near the electrode:

$$\tau_s = \pi D\left(\frac{FC_0}{2J(1-t_{\mathrm{Li}^+})}\right)^2 \tag{6}$$

where J is effective current density and C_0 and D are the bulk concentration of electrolyte and salt diffusion coefficient, respectively, and t_{Li^+} is the Li^+ transference number. The continuous plating beyond a critical current (J^*) in a cell with the electrodes' spacing of l leads to the ion depletion as early as τ_s:

$$J^* = \frac{2FC_0D}{l(1-t_{\mathrm{Li}^+})} \tag{7}$$

The observation of dendrite growth at currents below this threshold (J^*) but with an induction time yet proportional to the Sand's time was explained by the non-uniform distribution of current in-plane of the electrode triggered by the possible surface inhomogeneities and passivation layers.[60]

Monroe and Newman[6] improved the earlier model of Barton and Bockris,[58] by considering the transient changes in the potential (Φ) and concentration (C) near a growing Li dendrite tip. They assumed a binary dilute electrolyte and neglected any violation of electroneutrality at the interfaces. Consistent thermodynamic reference points were used to define the surface overpotential ($\eta = \Phi_1 - \Phi_3$) at the dendrite's tip (Figure 3a). Particularly, the surface forces were explicitly introduced into a modified Butler-Volmer (BV) kinetics as the equilibrium potential difference between the dendrite tip and a hypothetical adjacent planar Li reference electrode:

$$(\Phi_1 - \Phi_2)_{\mathrm{eq}} = -\frac{2\gamma V}{rF} \tag{8}$$

$$\frac{i}{i_{0,\mathrm{ref}}} = \frac{\exp\left(\frac{2\gamma V}{rRT}\right)\exp\left(\frac{\alpha_a F\eta}{RT}\right)-\exp\left(\frac{-\alpha_c F\eta}{RT}\right)}{\left(\frac{c_{ref}}{c_{Li+}^{\delta'}}\right)^{\alpha_a} + \frac{(1-t_{\mathrm{Li}^+})ri_{0,\mathrm{ref}}}{FDc_{Li+}^{\delta'}}\exp\left(\frac{-\alpha_c F\eta}{RT}\right)} \tag{9}$$

where i is the current density normal to the dendrite surface, α_a and α_c are the anodic and cathodic transfer coefficients, and $i_{0,\mathrm{ref}}$ refers to the value of exchange current density measured at a reference condition (c_{ref}). The growth velocity of dendrite (Equation 2) was then simulated and unlike previous works showcased to be non-constant and to accelerate during the galvanostatic plating of lithium. Later on, Monroe and Newman[61,62] presented a thermodynamically consistent model to account for the impact of elastic, viscous, and external pressure forces next to the surface tension on the kinetics of Li plating for a deformed electrode/electrolyte interface (Figure 3b). This was a significant progress compared to the previous models in which the mechanical effects were only limited to the surface tension at the dendrite/electrolyte interface. The essence of this elegant model of Monroe is to relate the difference between the electrochemical potential of electrons at the deformed (α) and undeformed (α') parts of the Li electrode ($\Delta\mu_{e-}^{\alpha,\alpha'}$) to the deformation-induced pressure differences at the both sides of the interface, i.e. Li ($\Delta p^{\alpha,\alpha'}$) and electrolyte ($\Delta p^{\beta,\beta'}$):

$$\Delta\mu_{e-}^{\alpha,\alpha'} = \overline{V_{Li}}\Delta p^{\alpha,\alpha'} - \overline{V_{Li+}}\Delta p^{\beta,\beta'} \tag{10}$$

where $\overline{V_{Li}}$ and $\overline{V_{Li+}}$ stand for the partial molar volumes of Li metal and lithium ions, respectively. Integrating the force balance across the Li/electrolyte interface with Equation (10) will expose the deformation ($\underline{\tau}_d$) and viscous ($\underline{\tau}_v$) stress tensors, with a convention of positive compressive stress, and the mean curvature of the interface ($\mathcal{H}$) in the following equation:

$$\Delta\mu_{e-}^{\alpha,\alpha'} = -\left(\frac{\overline{V_{Li}}+\overline{V_{Li+}}}{2}\right)\left\{2\gamma\mathcal{H} + \underline{e}_n^{\alpha}.\left[\underline{e}_n^{\alpha}.\left(\Delta\underline{\tau}_d^{\alpha,\beta} + \Delta\underline{\tau}_v^{\alpha,\beta}\right)\right]\right\} + \left(\frac{\overline{V_{Li}}-\overline{V_{Li+}}}{2}\right)\left(\Delta p^{\alpha,\alpha'} + \Delta p^{\beta,\beta'}\right) \tag{11}$$

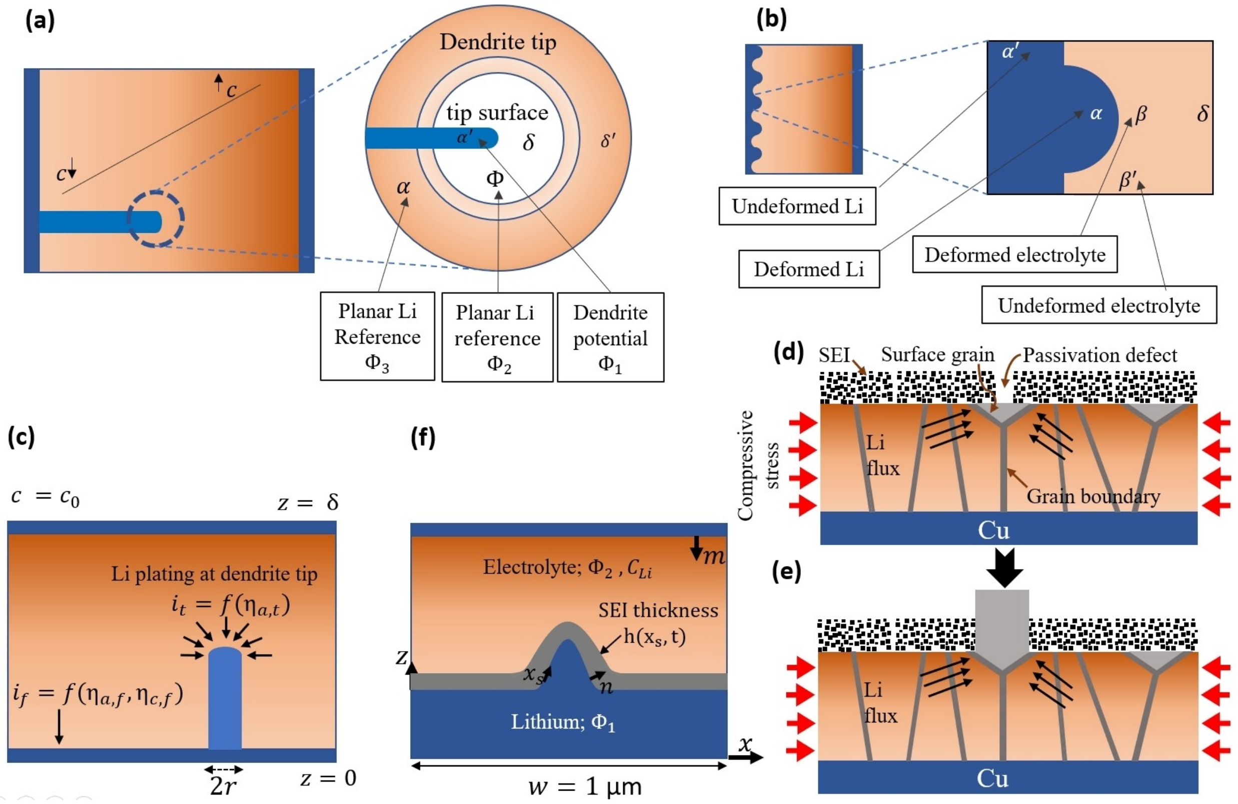

Figure 3. Different concentration and potential regions around a growing dendrite tip (**a**) with and (**b**) without consideration of the deformation effects described by Monroe and Newman,[61,62,64] (**c**) schematic of the electrode surface on which Li is deposited according to Akolkar's model,[63] (**d**) Wang et al.,[65] plating-induced stress mechanism for dendrite growth due to the stress-driven diffusion flux of Li towards the base of a surface grain (**e**) forming a Li dendrite. (**f**) the schematic of the physical picture of dendrite penetration through the SEI layer proposed by Liu et al.[66]

where $\underset{-n}{e^{\alpha}}$ is the unit normal vector of the plane at the deformed Li surface pointing towards the electrolyte. The roughening kinetics of the Li/electrolyte interface was then derived considering the mechanical impacts and transport limitations, for a deforming interface, on the energetics of the Li plating and stripping:

$$i = i_{0,\mathrm{ref}}\left(\frac{c^{\delta}_{Li+}}{c_{\mathrm{ref}}}\right)^{\alpha_a} \exp\left[\frac{(\alpha_m-\alpha_a)}{RT}\Delta\mu^{\alpha,\alpha'}_{e-}\right]\cdot\left[\exp\left(\frac{\alpha_a F}{RT}\eta\right)-\left(\frac{c^{\beta}_{Li+}}{c^{\delta}_{Li+}}\right)\exp\left(-\frac{\alpha_c F}{RT}\eta\right)\right] \tag{12}$$

where α_m is a mechanical transfer coefficient representing the fraction of the mechanically induced electrochemical-potential difference that contributes to the activation energy of a deformed Li/electrolyte interface.

Akolkar[63] modeled the current density at the dendrite tip (i_t) as a multiple of the current density at the flat surface of the lithium electrode, i_f (Figure 3c). The simplified model neglects the concentration overpotential and surface forces at the dendrite's tip and further assumes that the overpotential at the dendrite and the flat surface of the electrode is equal. A stagnant Nernst diffusion boundary layer with the thickness of δ is assumed near the electrode surface with a concentration-dependent diffusion coefficient $D = ae^{-bc}$ where a and b are temperature dependent.

$$i_t = i_f\left[\frac{-1}{bc_0}\ln\left[e^{-bc_0}+\frac{i_f}{i_{L,f}}\left(1-e^{-bc_0}\right)\right]\right]^{-\alpha_c} \tag{13}$$

In this model the dendrite growth rate is sensitive to the electrolyte bulk concentration (c_0), the cathodic charge transfer coefficients (α_c), and the limiting current density for the flat electrode ($i_{L,f}$). In a following study, Akolkar[52] further incorporated the effect of the temperature in his model and concluded that at a given applied current density, there exists a critical temperature above which the formation of dendrites is inhibited.

2.2. Root-Controlled and Transition to Tip-Controlled Growth

Dendrite formation occurs even at low current densities, with two distinct structures: dense filaments or mossy Li and branched fractals known as dendritic Li. Koshina et al.[67] reported that at relatively low current densities and high salt concentrations, mossy Li is formed on the surface of Li anode. Other investigations on tin deposition evidenced the growth of tin whiskers from the base and not from the tip[68,69] due to the generated stress in the tin substrate. Arakawa et al.[70] were the first to report that Li dendrite can grow from the base of the substrate. These observations inspired Yamaki et al.[71] to investigate the formation of Li whiskers at low current densities, postulating that the stress in the substrate initiates growth of whiskers. In this regard, they proposed the following mechanism for the formation of Li whiskers based on the experimental observation in a symmetric Li cell with EC/2MeTHF/$LiAsF_6$ electrolyte. The deposition of lithium beneath the SEI layer is non-uniform and generates mechanical stress. This stress drives the transport of lithium through the grain boundaries, against the opposing surface tension forces at the interface, in order to relieve the stress. At a certain point, the SEI will break locally and the lithium whiskers are extruded out of the resulting holes in the SEI. They further proposed a phenomenological model to relate the morphology of the lithium deposit to the surface tension (γ) and the internal pressure of the deposit layer (ΔP). Particularly, it was hypothesized that different values of $\frac{\Delta P}{\gamma}$ relative to the creep strength of the lithium whisker can result in different deposit morphologies. An important implication of this model was that Li deposit adopts an amorphous particular morphology when the surface tension is strong enough to deform the Li whiskers. After 2 decades, these findings of Yamaki et al.[71] was developed further by Wang et al.[65] who conceptualized the impact of lithium plating-induced stress on the morphology of the deposits (Figure 3d and e). They experimentally showcased the role plating-induced compressive stress in the promotion of dendrite growth and proposed a model to contrast the Li plating on the soft and hard substrates. They observed the wrinkling of the soft substrates as a stress relief mechanism disfavoring the formation of Li dendrites. A model was proposed according to which the dendrite formation begins when the Li filament growth rate, ν_{filamnet}, exceeds the rate of the uniform Li deposition:

$$\nu_{\text{filamnet}} = \frac{D_{\text{Li}} V_{\text{Li}} \sigma}{RTr} \tag{14}$$

where D_{Li} is the Li diffusivity in the deposit, V_{Li} is the molar volume of Li, σ is the compressive stress, and r is the filament's radius. Based on this model, a critical compressive stress, σ_{crit}, can be obtained for a given plating current density (i) below which the Li dendrite formation is mitigated:

$$\sigma_{crit} = \frac{RTr}{FD_{\text{Li}}} i \tag{15}$$

The in-situ experiments[72–74] revealed that the growth of deposited Li in liquid electrolytes undergoes a transition point wherein the root growth mechanism shifts to a tip growth mechanism. Utilizing an in-situ optical setup, Bai et al.[74] demonstrated that during the initial stages of electrodeposition, mossy Li grows from its roots, evident by the tip of the deposition retaining its shape over time. However, at the voltage spike, dendritic Li structures were observed growing from the tip. Given that dendritic growth typically signifies diffusion-limited aggregation, the experimental time to reach the voltage spike was postulated as the Sand's time, with Equation (6) employed to derive an apparent diffusion coefficient. Interestingly, the calculated diffusion coefficient aligned with the reported measured diffusion coefficients for the similar systems. Bai et al.[74] similarly demonstrated that the typical operating current densities of LIBs favor mossy Li growth over dendritic growth. Mossy growth, characterized by the accumulation of Li whiskers, is conventionally associated with reaction limitations. To delve deeper, Kushima et al.[75] conducted additional research on Li nucleation and growth through in-situ environmental transmission electron microscopy (ETEM) to highlight the significance of SEI formation in Li growth. They identified two growth modes within the reaction-limited region, preceding Sand's era and the onset of diffusion-limited dendritic growth. The first mode involves Li deposition resembling cauliflower or Eden-like clusters on the electrode surface, likely a mixture of tip and root growth mechanisms. The second mode manifests as whisker-like Li growth, a consequence of the competition between SEI growth and Li deposition. This mode is controlled by the root growth mechanism in line with the Kushima et al.'s proposed mechanisms[75] and the theoretical findings of Yamaki et al.'s.[71] Here, stress accumulation beneath the SEI layer prompts its rupture at certain points, enabling Li whiskers to emerge through the resulting holes as a stress-relieving mechanism.

Liu et al.[66] developed a model describing Li dendrite growth, SEI formation, dendrite penetration through the SEI layer, and the regrowth of SEI on the Li exposed surface (Figure 3f). To do so, the total applied current density (i_t) was split into the Li deposition current density (i_{Li}) and the current density consumed for the formation of SEI (i_{SEI}):

$$i_t = i_{\text{Li}} + i_{\text{SEI}} \tag{16}$$

The overpotential used in the kinetics equation was corrected to incorporate the effect of the SEI layer and also the stress on the substrate surface while the surface energy effects were neglected:

$$\eta = \Phi_1 - \Phi_2 - R_{\text{SEI}} i_t - U_{eq} - \frac{V_{\text{Li}} \sigma_{hs}}{F} \tag{17}$$

where Φ_1 and Φ_2 correspond to the Li electrode and electrolyte potential respectively, U_{eq} is the equilibrium potential, and σ_{hs} is hydrostatic stress. R_{SEI} is the resistance of the SEI layer and is estimated according to the growth and the stretchability of the SEI layer which depends on its strain rate.

Inspired by the works of Ferrese and Newman,[76,77] Jana et al.[78,79] extended the thermodynamic framework of Ely and Garcia[80] considering elastic energy contributions and Li plastic deformation. Their model identified five distinct regimes of dendrite growth, aligning with the experimentally observed dendrite growth morphologies reported in the literature. These five regimes include: (1) thermodynamic suppression regime, (2) incubation regime, (3) based-controlled growth regime, (4) tip control growth regime, and (5) mixed growth regime. In the thermodynamic suppression regime, the Li embryos are energetically unstable and tend to dissolve back into the electrolyte. The incubation phase is defined as the time required for thermodynamically stable electrodeposits to enter the stable growth regime. Jana et al.[78,79] showed that the different regimes of Li electrodeposition can be well predicted by a dimensionless applied current and a dimensionless electrodeposit size. Their result showed that for relatively low current densities and above the kinetic limits, the Li plasticity at the base controls the electrodeposition, i.e., based-controlled regime. Above a critical current density which depends on the material properties of a specific system, diffusion limitations induce the formation of high-branched dendrites that correspond to tip-controlled regime. In the mixed growth regime, plastic deformation and electrodeposition have significant contributions. A chronological summary of the discussed dendrite growth models is presented in Table 2. The dendrite growth mitigation solutions corresponding to each specific model are presented in this table.

3. Computational Insights

Due to the complexity of the underlying phenomena in Li electrodes and their varying time and length scales, a multiscale approach combining various computational methods is necessary to capture the intricate behavior of Li electrodeposition. These methods range from quantum chemistry (QC) calculations,[83] which probe atomic interactions and electronic structures, to molecular dynamics (MD) simulations[84] that model the dynamic behavior of atoms and molecules, to kinetic Monte Carlo (KMC) simulations[84] that explore the stochastic nature of chemical reactions, and finally, to macro-scale simulations[6,85] that encompass larger-scale electrochemical phenomena (Table 3).

3.1. Dendrite Formation

In this context, dendrite formation and its influencing factors have been investigated using computational and simulation methods across different time and length scales. QC calculations are employed to determine the energy gap between Li bulk and crystal surfaces.[86–89] A comparison of the energy gap for Li with its alternatives, Na and Mg, indicates that a comparatively low energy gap leads to a tendency for Li atoms to create one-dimensional structures, such as whiskers[90] (Figure 4a). Detailed calculations have shown that this tendency arises from weak interactions among Li atoms in the crystal lattice.[86] From a thermodynamic viewpoint, the formation of surfaces with low free energy is favorable. As a result, deposition is expected to lead to Li growth on facets with the lowest free energy.[20] Hagopian et al. performed[91] QC calculations based on surface tension as a function of the operating potential of the Li anode. Their results have shown that the facet (110) has the lowest free energy and exhibits the highest growth at operating voltages higher than the point of zero charge. A further decrease in the operating potential of the Li anode would make other facets thermodynamically stable, potentially leading to the creation of mossy and fractal structures. However, another QC investigation[92] and a study at a higher length scale by using KMC simulations,[93] have depicted that kinetic factors can play a critical role in dendrite formation, in addition to thermodynamic factors. While the KMC results agree with thermodynamic expectations at low deposition rates, their deviation increases at high deposition rates. Ghalami Choobar et al.[93] attributed this behavior to the fact that facets with higher energy participate in deposition reactions, and Li cations are deposited on these surfaces. However, when the deposition rate is low, there is enough time

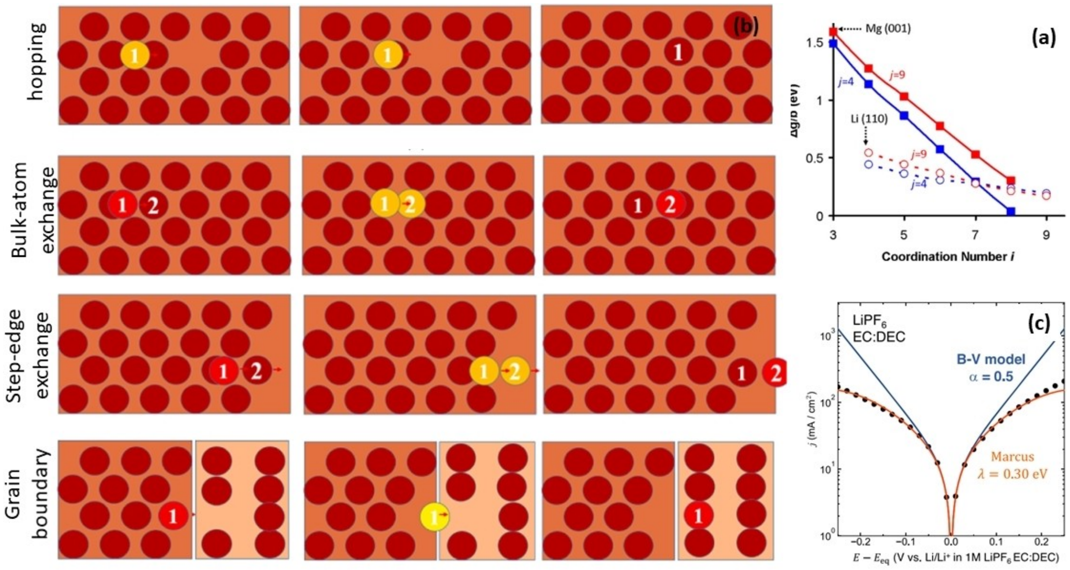

Figure 4. (**a**) Free energy change for different coordination numbers of the adsorbed atom for Li and its comparison with Mg,[90] Copyright 2012, Elsevier (**b**) schematic representation of various surface diffusion mechanisms: hopping, bulk-atom exchange, step-edge atom exchange, and grain boundary mechanisms,[93] Copyright 2021, Elsevier and (**c**) comparison of experimental data for kinetics of Li surface against BV and Marcus model,[96] Copyright 2020, American Chemical Society.

Table 2. A chronological summary of some of the main dendrite growth models based on tip-controlled, root-controlled, and tip and root mixed-controlled mechanisms.

Model	Mechanism	Key assumptions	Main outcomes	Suggested dendrite mitigation solution
Barton and Bockris[58] 1962	Tip-controlled	Linear electrochemical kinetics Static hemisphere dendrite Inertial and mechanical forces are ignored	Identification of a concentration-dependent critical current density above which dendrites from The number of dendrites correlates with the applied current density	Dendrite growth can be prevented by decreasing overpotential
Chazalviel[59] 1990	Tip-controlled	The developed space charge near the anode surface is the driving force for dendrite formation The model only applies above limiting current density	The onset of nucleation is inversely proportional to the square of the effective current density The dendrite growth rate is proportional to the anion mobility	Dendrite dense branching can be minimized by reducing the electric field
Yamaki[81] 1998	Root-controlled	Stress in the substrate as the driving force for dendrite formation	Depending on $\frac{\Delta P}{\gamma}$ values, three deposition morphologies were identified	Strong surface tensions can result in particle/amorphous deposits
Monroe and Newman[6] 2003	Tip-controlled	The transient behavior of a parallel electrode system is studied The dendrite is small enough that does not affect the potential and concentration profiles	The rate of dendrite growth increases with charging time Surface forces show little effect on dendrite growth	Increasing interelectrode distance can postpone cell failure
Ely and Garcia[80] 2013	Root-controlled	Model applied for early-stage nucleation of reaction-limited systems	For a nucleus to enter the growth phase, its size must be larger than both the thermodynamic and kinetic critical radii Embryos nucleate at interfacial heterogeneities	Dendrite formation can be suppressed by controlling (1) the anode surface roughness, (2) anode particle size, (3) plating potential, and (4) wettability properties of the surface
Akolkar[63,82] 2013 and 2014	Tip-controlled	Concentration-dependent diffusion coefficient A stagnant Nernst diffusion boundary layer exists near the electrode surface dendrite growth is solely governed by the activation mode	The dendrite growth rate depends on electrolyte concentration, applied current, and kinetics	A critical temperature was identified above which dendrite formation is inhibited
Liu[66] 2017	Tip and root mixed-controlled	Dendrite growth was coupled with SEI formation Effect of surface energy was neglected	While working at relatively low current densities, increasing the current facilitates dendrite growth while maintaining the dendrite shape. At relatively high current densities, increasing the current not only results in faster dendrite growth but also form sharp needle-shaped dendrites. SEI with a lower resistance can mitigate the formation of sharp needle-shape dendrites. The inhomogeneities and defects in the SEI structure can induce dendrite formation even though the surface of the lithium electrode is perfectly flat.	A flat initial lithium surface and a low-resistance uniform SEI layer reduce the dendrite formation and growth rate
Wang[65] 2018	Root-controlled	The model applies to early-stage Li dendrite growth Stress in the substrate as the driving force for dendrite formation	dendrite formation begins when the lithium filament growth rate, $\nu_{filamnet}$, exceeds the uniform lithium deposition rate, $\nu_{plating}$	A critical compressive stress, σ_{crit}, exists below which the Li dendrite formation is mitigated
Jana[78,79] 2017 and 2019	Tip and root mixed-controlled	The bulk free energy of transformation includes contributions from electrical, chemical, and mechanical sources. The plastic deformation of lithium is described by a power law creep model	Five regimes of dendrite growth were identified as a function of a normalized current density and normalized electrodeposit size At the typical current density ranges for lithium-ion batteries, dendrite growth is governed by a combination of mixed-base and tip-control mechanisms.	Maximizing the hydrostatic share of the stresses, and minimizing the deviatoric share can suppress dendrite growth

for the electrode to relax and form surfaces with the lowest free energy through surface diffusion mechanisms (Figure 4b). Li exhibits a higher surface diffusion barrier compared to other metals which may impede the formation of a smooth, uniform surface during deposition. Although various thermodynamic models exist to describe the behavior of the Li electrode, the

Table 3. Comparison of computational methods in the application of Li electrode simulation.[6,83–85]

Computational methods		Force Field Type	Strengths	Weaknesses	Applications	Computational Efficiency
Quantum Chemistry (QC) Calculation		Quantum mechanical potential	Provides highly accurate electronic structure information	Very expensive; limited to small systems and very short time scales	Calculating accurate energies, studying reaction mechanisms	Very Low
Molecular Dynamics (MD) simulations	Classical MD	Classical potential	Efficiently simulates large numbers of atoms	Limited to studying systems with non-breaking bonds; cannot capture electronic processes	Ion transport in electrolytes, diffusion phenomena	High
	Ab Initio MD	Quantum mechanical potential	Provides high accuracy for chemical bonds and reactions	Expensive; limited to simulating small systems and short time scales	Investigating chemical reaction mechanisms at electrode surfaces; understanding interfacial phenomena	Low
	Reactive MD	Reactive potential	Can simulate bond-breaking and formation	Computationally expensive; requires careful parameterization of the force field	Simulating electrode-electrolyte interface dynamics, including reactions like Li plating/stripping	Medium
	Coarse-Grained MD	Coarse-grained potential	Simulates large spatial and temporal scales	Lower accuracy compared to atomistic simulations	Simulating polymer electrolyte dynamics, morphology evolution	High
Kinetic Monte Carlo (KMC)		Classical potential	Simulates rare events and longtime scales	Requires accurate rates for all possible processes	Modeling nucleation and growth of SEI layers, studying battery degradation	Medium
Phase Field Modeling (PFM)		Phase field equations	Can simulate complex morphologies and microstructure evolution	Requires careful parameterization of the free energy functional	Simulating dendrite growth, and phase separation in cathode materials	Medium to High
Macro Scale Simulation		Continuum equations (e.g., FEM, FVM)	Simulates large-scale systems and considers mechanical, and thermal effects	Less detailed than atomistic simulations	Modeling battery packs, simulating thermal runaway	High

Butler-Volmer (BV) model[6] has been extensively employed to represent surface reactions during simulations, which fails at states far from equilibrium with non-Boltzmann distributions.[94] In this regard, a theoretical framework based on Marcus kinetics has been developed to address the shortcomings of the BV model.[95] Experimental and simulation results have indicated that the BV model suffers from reaction rate overestimation, disagreement with experimental results, and symmetrical response during plating/stripping.[96,97] The Marcus theory can resolve these issues and also take into account the electronic structure of the electrode and the molecular construction of the electrolyte.[96–99] (See Figure 4c).

Furthermore, thermodynamic and kinetic tendencies can be affected by surface roughness and the formation of tip points, in addition to intrinsic characteristics. This point has been elaborated on in further detail by calculating potential and partial charge distributions.[100–103] KMC simulations have shown that tips experience a higher rate of reactions due to changes in the potential distribution in the electrode and electrolyte.[101] Santos and Schmickler[100] confirmed this observation by determining the partial charge distribution through QC calculations. They showed that an extra partial charge on an atom at the tips can affect the charge distribution on the four atoms surrounding it. A scrutinized dissection of the results indicates that the electric field induced by a higher partial charge density at the tips affects its nearby surrounding, due to the screening properties of the electrolyte and electrode (Figure 5a and b). This observation aligns with the aspect of dendrite growth on tips presented in the previous section. Further investigation of the Li crystal under the effect of an external electric field confirms the screening property of the Li electrode since the surface diffusion activation energy has changed negligibly.[87] Aryanfar[104] utilized KMC to study the impact of surface curvature on deposit roughness illustrating that a convex surface is less prone to form dendrites due to the absence of spatial hindrance compared to flat electrodes (Figure 5c and d). From another perspective, phase-field modeling showed that surface roughness impacts the electrode and electrolyte contact by creating contact resistance to ion transportation.[105] This observation was also confirmed by solving continuity equations, where results showed a decrease in ion transport in the holes, which intensifies uneven surface growth.[106]

3.2. Electrolyte Stability and SEI Formation

The effectiveness of metallic Li electrodes is intricately linked to the electrolyte's composition and stability.[28,107] It is imperative that the electrolyte remains electrochemically stable upon contact with the electrode surface, facilitating efficient cation transfer. Variations in solvent type, salt, additives, and their respective concentrations can significantly influence these

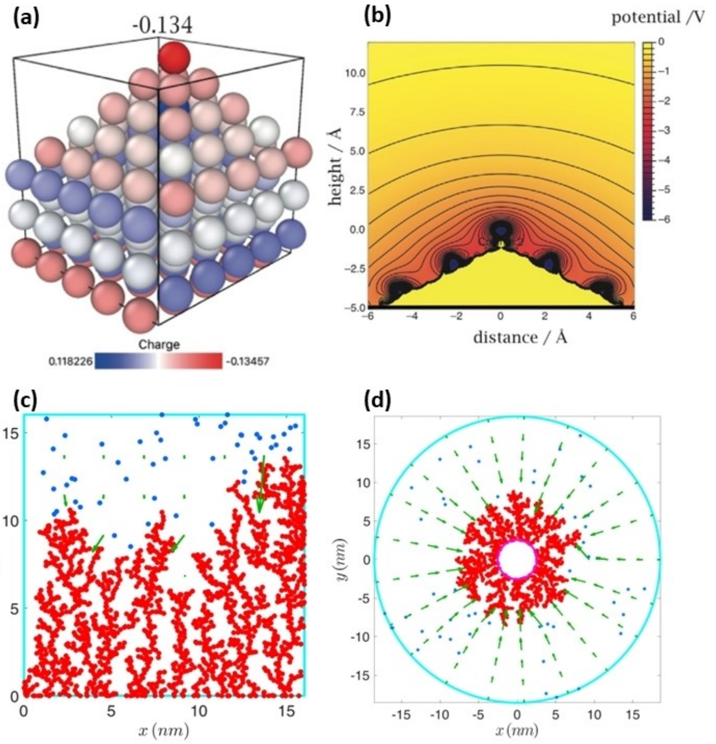

Figure 5. (**a**) Charge distribution and (**b**) electrostatic potential contours on a pyramidal tip for a Li electrode with an excess charge obtained by QC calculations,[100] Copyright 2021, John Wiley and Sons. Dendrite morphologies are grown on the (**c**) flat and (**d**) curved surface obtained by KMC simulation,[104] Copyright 2020, American Physical Society.

properties. QC techniques, particularly those assessing the Fermi level of the anode against the lowest unoccupied molecular orbital (LUMO) and highest occupied molecular orbital (HOMO), are utilized to analyze electrolyte stability on Li electrodes.[108] These QC analyses, which involve evaluations of the density of states (DOS) for the electrode and molecular orbital for existing species within the electrolyte, offer predictive insights into electrolyte stability, albeit without addressing SEI layer formation potential. Empirical data reveals that the common electrolyte, ethylene carbonate (EC) plus lithium hexafluorophosphate ($LiPF_6$), is prone to decomposition via four-electron reactions when in contacts with the Li anode.[109,110] Varying the anionic component by using alternative salts such as lithium bis(fluoromethanesulfonyl)imide (LiFSI) or lithium bis(trifluoromethanesulfonyl)imide (LiTFSI) facilitates a LUMO shift to the anion (See Figure 6a and b), thereby mitigating further electrolyte degradation by enabling electron acceptance and subsequent LiF layer formation.[109] Investigations indicated that reduction of molecular interties often involves a one-electron transfer to anion and its breakdown into ionic species, while oxidation is intricate since HOMO can be located on solvent or anion.[111] However, high salt concentrations are essential to maintain anionic presence within solvent-coated electrolyte structures, preventing solvent degradation during the charging cycle. High-concentration electrolytes exhibit a dominance of contact-ion-pair (CIP) and Aggregate (Agg) species over solvent-separated-ion-pair (SSIP) configurations.[27,112] QC investigations into (Trimethyl phosphate) TMP-based electrolytes with LiFSI salt have discerned that $Li(TMP)_3FSI$ and $Li(TMP)_4$ represent the most and least stable molecular entities, respectively, suggesting accelerated electrolyte decomposition at low salt concentrations.[113] Beyond analyzing anionic effects, enhancements in solvent molecular structure aimed at enhancement of electrochemical stability or transport attributes are achievable through QC and MD simulations. Such studies alongside experimental studies have confirmed the superior stability of ether solvents when utilized with metallic Li anodes.[107] QC calculations[113] and MD simulation[29,114] have revealed that the solvent fluorinated 1,4-dimethoxylbutane (FDMB) demonstrates exceptional compatibility with the metallic Li anode. This favorable interaction is attributed to the CF_2 functional group within the solvent's molecular structure, which facilitates a stable solvation environment for the Li ions. The CF2 group's electron-withdrawing properties enhance the solvation process, leading to a more uniform and durable electrode-electrolyte interface.[29,113] Moreover, solid electrolytes formulated from poly(ethylene oxide) (PEO) and LiTFSI salt have been studied through molecular simulations for their superior physical and mechanical properties, alongside their dendrite mitigation capabilities. Initial calculations confirm the stability of high molecular weight PEO on the Li anode surface.[115] Scrutinized analysis of radial distribution function (RDF) indicated the spatial hindrance, posed by the macromolecule's extended chain structure, promotes anion-cation interactions in the vicinity of the anode, thereby enhancing CIP species prevalence within the solid

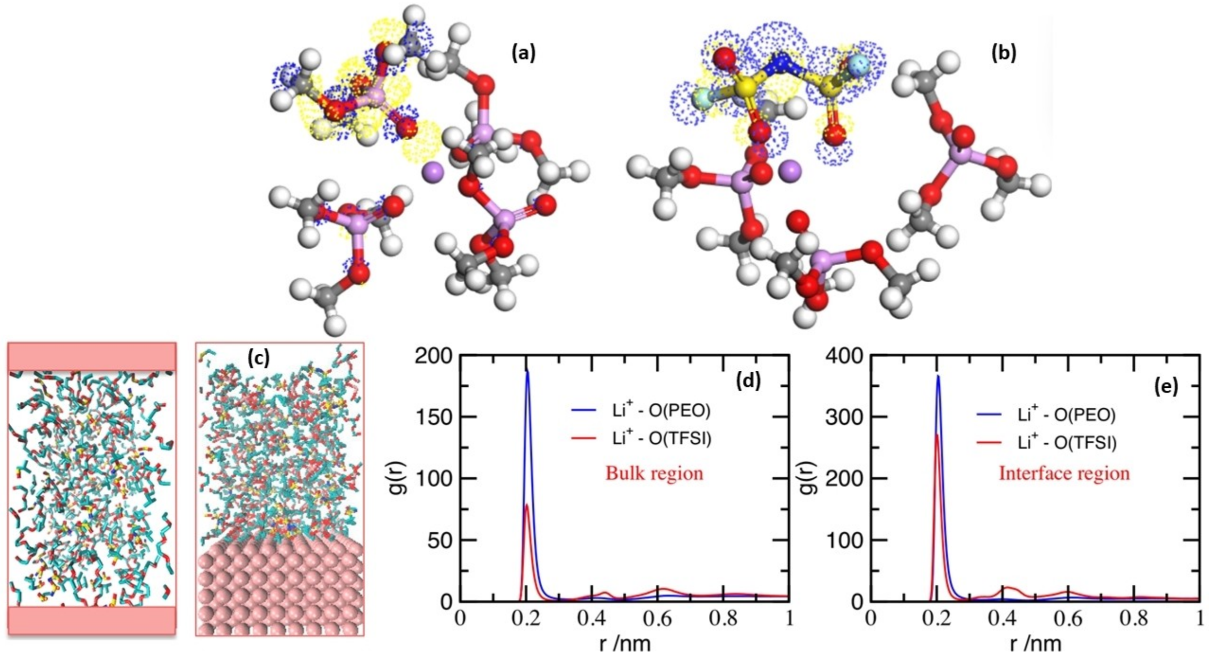

Figure 6. Visualization of optimized molecular configurations and electronic properties: (**a**) The optimized molecular structure of Li(TMP)$_4$ and (**b**) Li(TMP)$_3$FSI, showcasing the LUMO as determined by QC calculations employing the B3LYP functional within Gaussian software.[118] (**c**) Detailed molecular illustration depicting the simulation of the PEO+LiTFSI electrolyte system proximal to the Li electrode. (**d**) RDF analysis for the Li–O pair interactions within the bulk electrolyte matrix. (**e**) RDF plot highlighting the Li–O pair dynamics at the critical electrode-electrolyte interface, elucidating the interfacial structure and ion transport mechanisms,[116] Copyright 2017, Elsevier.

electrolyte matrix[116] (Figure 6c–e). While this phenomenon contributes to the electrolyte's electrochemical stability, it simultaneously hinders Li ion transport toward the anode. Ionic conductivity enhancement, coupled with improved physical compatibility and diminished contact resistance, can be achieved through the application of various additives, including ionic liquids and salts. The addition of salts like potassium Bis(fluorosulfonyl)imide (KFSI) and KPF$_6$ not only enhances ionic conductivity but also plays a role as a cationic barrier, due to the presence of metal cations such as Na and K within the electrolyte. Hao et al.[101] used KMC simulation to demonstrate that the presence of these cations initiates competitive interactions with Li cations during the plating process. Their integration within the deposit structure fosters enhanced surface diffusion through the formation of interstitial defects[117] within the crystal lattice, thereby promoting the formation of smoother surfaces throughout the battery charging process. Concurrently, the lower mobility and reactivity of these ions ensure a more uniform distribution within the electrolyte, leading to a uniform electrochemical plating reaction rate across the electrode surface.

The SEI layer plays a crucial role in LMBs, analogous to its function in LIBs, where its absence significantly reduces battery life. The presence of the SEI layer leads to a voltage drop due to resistive losses. Moreover, its composition, thickness, and porosity greatly influence the rate of Li deposition. To investigate the formation of this layer and its performance based on its constituents, MD and KMC simulations are employed where the former focus on molecular interactions and provides various details from the mechanism of formation to the interaction of Li with the SEI layer components during deposition.[119] On the other hand, the latter concentrates on larger-scale phenomena such as the impact of SEI stiffness on the distribution of deposition reactions and the probability of dendrite formation. Classical MD simulations have been used to study Li-ion transport in artificial SEI layers made of Li$_3$P and Li$_2$S.[120] Their results indicate that Li$_2$S is superior due to its higher ionic conductivity. Additionally, the presence of vacancies and defects in the SEI's crystalline network can significantly reduce resistive losses by increasing the hopping diffusion mechanism. Another study on the physical and mechanical properties of an artificial layer of Li$_{2-x}$O$_{1-x}$F$_x$ showed that Li could be trapped by oxygen.[121] Therefore, with a higher number of fluorine atoms, the ionic conductivity of the layer improves without a significant reduction in Young's modulus. Moreover, MD simulations with the capability to model bond formation and breakage have been extensively used to investigate the formation of this layer (see Table 3[78–80] to compare various versions of MD simulation). A computational study using Ab Initio MD simulations showed that in an EC+LiPF$_6$ electrolyte solution, the SEI layer does not form.[110] Galvez-Aranda et al.[122] have shown that the presence of the FSI$^-$ anion, along with its subsequent decomposition, results in the consumption of 17 Li ions. This process yields a variety of chemical species. Notably, the formation of LiF and Li$_2$O is observed among these species. The presence of these compounds is indicative of the formation of a SEI layer. A computational comparison of FSI and TFSI anions using QC indicates that the FSI anion is more prone to layer formation.[123] This behavior is attributed to the lower stability of this anion and the fact that it releases more fluorine atoms. The released fluorine reacts with Li cations to form the LiF layer, which has desirable mechanical and transport properties as an SEI layer. Additionally, MD simulations based on the ReaxFF force field showed that adding HF to electrolytes can significantly aid in the formation of this layer by decomposing and creating fluoride ions.[124] In another reactive MD simulation study, Zhou et al. examined the effect of pressure on the density of the formed SEI layer.[125] It was shown that increasing pressure increases the density of the layer and reduces its porosity. Although this observation reduces dendrite formation, it also affects the diffusion coefficient of cations. Therefore, it is necessary to select an optimal value for the operational pressure.

4. Perspectives on Computational-Experimental Synergy and Future Directions

The synergy between computational and experimental approaches offers a powerful framework for unraveling the complexities of Li metal electrodes and to devise mitigation strategies. This collaborative approach not only accelerates the discovery of novel materials but also refines our understanding of dendrite formation, electrolyte interactions, and ion transport phenomena. Computational models, based on the theoretical chemistry and physics, provide a window into the atomic-level interactions and processes that are often intangible in experimental setups. They allow us to simulate various scenarios and predict outcomes, offering insights that guide experimental design and interpretation. On the other hand, experimentation serves as a critical reality check for computational models, ensuring their relevance and accuracy. In this section, we highlight the pivotal role of computational-experimental synergy in advancing the Li metal electrode research and the prospective pathways for the continued advancement of Li metal electrode technology (Figure 7).

The good match between the predictions of the dendrite growth models (Section 3) and the experimental data exemplifies the power of physics-based models in the quantitative interpretation of the Li electrode performance. For instance, Pei et al.[126] conducted SEM analysis to study the morphology of deposited Li during the early stages of nucleation and growth. Their observations demonstrated that the size, shape, and density of the formed nuclei depend on current density, identifying a critical current density aligned with the thermodynamic suppression regime described in Ely's and Jana's models.[78–80] Below this critical current density, dendrite formation is suppressed. Also, they showed that the nuclei size is inversely proportional to the overpotential, which clearly confirms the predictions of Ely's model.[80] Such specialized experiments focusing on the early-stage nucleation and growth of Li deposits are crucial for proposing dendrite mitigation strategies.

It is well accepted that three phenomena play a crucial role during battery charging and Li plating: ion transfer in the electrolyte, surface electrochemical reaction, and surface diffusion. If these phenomena are not balanced, structures such as whiskers or dendrites will form instead of smooth and even surfaces. To investigate and quantify these competitions, dimensionless numbers and sensitivity analysis offer valuable tools. Dimensionless numbers serve as powerful analytical tools for comparing physical and chemical parameters across diverse

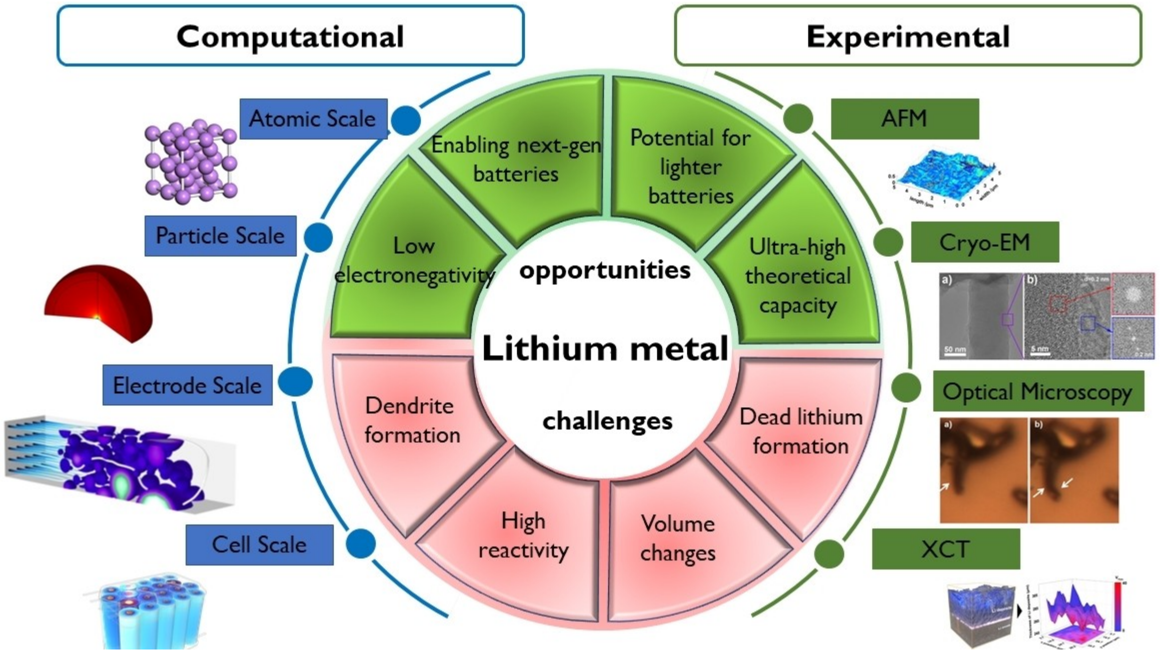

Figure 7. The power of combined methods to overcome the remaining challenges of the Li metal electrodes. Reproduced with permission,[24,47,156–158] Copyright 2017, American Chemical Society, Copyright 2018, American Chemical Society, Copyright 2021, American Chemical Society, Copyright 2017, Elsevier, Copyright 2014, Elsevier.

systems. Particularly relevant dimensionless numbers for Li electrode studies include the Wagner number,[127] the transport number,[128,129] the Damkohler[101,130] number, and the dimensionless time number.[131] By analyzing these dimensionless groups, rather than performing expensive experiments and subsequent analysis, researchers can gain deeper insights into the factors governing Li plating behavior and establish design principles for optimizing Li electrode performance. For instance, the Chazalviel model[59] and particularly Equation (7) suggest that a high transport number (the ability of Li ions to move through the electrolyte compared to other ions) is beneficial for mitigating dendrite formation. Therefore, scientists should focus on developing materials and strategies to enhance the transport number within the electrolyte. On the other hand, sensitivity analysis studies[132,133] have revealed that the rate of electrochemical reactions is more sensitive to temperature changes compared to other parameters. Results from the KMC simulation by Vishnugopi et al.[133] suggest that at operational temperatures around 75°C, an increase in both ion transfer rates within the electrolyte and surface diffusion rates at the electrode can inhibit the formation of dendrites. This phenomenon, referred to as "self-healing," has been consistently observed in experimental settings.[134,135] Moreover, the temperature range at which self-healing occurs can be effectively lowered through the molecular engineering of the electrolyte and by employing electrodes with a specifically designed crystal structure. From another perspective, dendrites begin to form when the local current density becomes so high that it overcomes surface diffusion, which can be examined by analyzing the order of magnitude of current density and surface diffusion.[93] To do this, assume that q_e is the charge of the incoming ions, and J and a are the current density and surface lattice constant, respectively. It is expected that dendrites will form when the average distance (d) traveled by a diffusing atom in the (average) time interval between two deposition events at a location ($t = q_e/(Ja^2)$) is smaller than the tip of the growing dendrite. Using analysis, it was shown that for a microscopic average distance (d) of about 10–300 micrometers, the diffusion activation energy that can enable a competitive rate of surface diffusion should be in the range of 0.05 to 0.15 electron volts. This idea has been implemented in various ways, such as a hybrid network of nanotubes,[136] defect engineering,[117] predefined crystal structure,[137] and surface engineering methods.[138]

Selecting a suitable and safe electrolyte for LMBs remains a challenge, with only a limited range of practical options. Electrolyte performance is highly dependent on operating conditions, with lower ionic conductivity and diffusion at lower temperatures,[27] while degradation reactions accelerate at higher temperatures.[139] Many traditional solvents used in LIBs become ineffective with the transition from graphite to Li metal anodes on account of the associated change in the operational potential of the anode.[109,110] In this context, the predictive power of QC calculations and MD simulations is crucial for developing new electrolytes. The electronic structure of electrolyte components and the comparison of their molecular orbital levels with the Fermi level of the anode determine the electrolyte's stability and its propensity to engage in oxidation and reduction reactions during battery charging and discharging. For instance, the introduction of HCEs and localized HCEs has always been a topic of interest. Molecular simulations have shed light on the underlying mechanisms based on molecular orbital transformations.[29,109,125] This has opened avenues for designing more suitable electrolyte components based on the molecular properties of the constituents. Additionally, molecular calculations have demonstrated that the presence of fluorine atoms in the electrolyte components and the electrolyte's ability to generate fluoride anions can extend battery life by facilitating the formation of a SEI layer composed of LiF.[29,109] Consequently, fluorinated solvents like FEC, and salts such as LiFSI and LiTFSI,[49,140] have garnered significant attention and are frequently used as primary components in electrolytes for current research. Experimental studies have shown that the performance of electrolytes in LMBs is strongly correlated with the relative amounts of organic, inorganic, and gaseous components formed during electrolyte decomposition.[44] The SEI layer in LMBs must be sufficiently flexible to withstand the stress from volume changes in the electrode. As a result, reactive computational methods like reactive MD and Ab Initio MD have become increasingly prominent.[21] While reactive molecular simulation offers valuable insights into LMBs, its computational expense has limited its widespread application. To address this challenge, machine learning methods have emerged as a promising avenue to accelerate LMB simulations, enabling more efficient exploration of complex electrochemical processes.[141,142] Moreover, solid-state and nanocomposite electrolytes have emerged as significant areas of research due to their safety benefits, suitable mechanical properties,[143] high electrochemical stability,[111] and superior transference numbers[144–146] compared to liquid electrolytes. In this context, machine learning has proven to be an effective tool for discovering novel electrolytes with tailored properties, thereby enhancing battery performance.[147]

Furthermore, computational methods can be highly beneficial for analyzing experimental results. The meticulous analysis of microscopic images (e.g., AFM, SEM, TEM) and complex spectra (e.g., XPS, XRD) using manual methods is time-consuming and prone to errors. Moreover, humans alone cannot accurately distinguish all the details of anode surface morphology and its various compounds. Additionally, human judgment can be influenced by various factors over time. As previously mentioned, both simulation[148] and experimental[47] results indicate that the initial structure and conditions of the electrode play a crucial role in its performance during the plating/stripping process. The accurate identification of the electrode's initial conditions based on experimental imaging results is also essential to assess its impact on electrode performance. In this regard, image processing methods have gained significant attention due to their ability to extract quantitative data from images.[149–151] For instance, image processing algorithms can be used to measure the size and distribution of dendrites or identify various chemical compounds on the electrode surface. On the other hand, with the generation of large volumes of numerical data from experimental images, the need for efficient computational methods for post-processing and analysis becomes imperative. Consequently, both supervised and unsupervised machine learning methods have been employed. For example, machine learning algorithms based on convolutional neural networks,[152,153] support vector machine and particle swarm optimization[154] can be utilized to classify microscopic images based on dendrite types or predict battery performance based on features extracted from images.[155]

As we continue to advance the frontiers of LMB technology, the integration of experimental and computational methods will become increasingly vital. The following multidirectional approaches are expected to accelerate the research and development of LMBs:

- **multiscale modeling**: current models primarily focus on specific phenomena (e.g., dendrite growth, electrolyte interactions) at specific time and length scales (e.g., atomic, microscopic). To gain deeper insights, multiscale models are required that can bridge the scales. This would result in a holistic understanding of Li metal behavior, considering the interplay between atomic interactions, microstructural evolution, and macroscopic battery performance.
- **machine learning for accelerated design**: machine learning algorithms can be further utilized to accelerate the design and discovery of novel electrode materials and electrolytes. By analyzing vast datasets of material properties and experimental outcomes, these algorithms can identify promising candidates and predict their performance with higher accuracy.
- **machine learning for accelerated simulation**: machine learning can significantly reduce the computational cost of high-fidelity methods like QC and MD simulations. This can be accomplished by employing machine learning to predict the properties of materials, thereby reducing the number of full simulations required. Also, machine learning can be used to create simplified models that capture the essential behavior of complex materials, allowing for faster simulations with good accuracy. This approach holds immense potential for accelerating the discovery and optimization of new electrode materials for LMBs.
- **operando characterization techniques**: traditional ex-situ characterization techniques provide snapshots of electrode behavior. The next step lies in developing robust operando techniques that can monitor critical processes like dendrite growth and SEI formation in real time during battery operation. This will provide invaluable insights for optimizing electrode design and electrolyte composition.
- **integration of high-throughput techniques**: high-throughput computational and experimental techniques coupled with machine learning can significantly accelerate the discovery of new materials. This could involve automated synthesis and characterization of electrode materials, followed by machine learning analysis to identify optimal candidates for further investigation.

5. Conclusions

A deep and quantitative understanding of the Li electrode behavior is necessary for the development of high-performance lithium metal batteries (LMBs). This insight cannot be achieved through isolated efforts, but rather demands a synergistic approach that exploits the strengths of both computational and experimental methods. The added value of such a synergistic approach was elaborated in this review paper. Particularly, the models of dendrite growth with different levels of sophistication were summarized and discussed. The good match between the experimental data and the model predictions underscores the importance of this synergy. For instance, the experimental data on the critical current density and the overpotential for the onset of dendrite growth was showcased to align with the theoretical predictions.

The future of LMB research lies in several promising directions. Multiscale modeling can bridge atomic, microscopic, and macroscopic scales, offering a comprehensive understanding of Li metal behavior. Machine learning techniques hold potential for accelerating the design and discovery of novel materials and for reducing the computational costs of high-fidelity simulations. The development of operando characterization techniques will provide real-time insights into critical processes during battery operation, further optimizing the electrode and electrolyte composition. By pursuing these approaches, researchers can unlock the full potential of Li metal electrode to develop high-performance, safe, and long-lasting LMBs.

Conflict of Interests

The authors declare no conflict of interest.

Data Availability Statement

Data sharing is not applicable to this article as no new data were created or analyzed in this study.

Keywords: Lithium metal batteries · Lithium electrode · Dendrite growth mechanisms · multiscale simulation · Characterization · Physics-based modeling

[1] K. Detka, K. Górecki, *Energies* **2023**, *16*, 5034.
[2] "Outlook for electric mobility–Global EV Outlook 2024–Analysis-IEA," can be found under https://www.iea.org/reports/global-ev-outlook-2024/outlook-for-electric-mobility, **n.d.**.
[3] H. Zhang, C. Li, G. G. Eshetu, S. Laruelle, S. Grugeon, K. Zaghib, C. Julien, A. Mauger, D. Guyomard, T. Rojo, N. Gisbert-Trejo, S. Passerini, X. Huang, Z. Zhou, P. Johansson, M. Forsyth, *Angew. Chem.* **2020**, *132*, 542.
[4] T. Wulandari, D. Fawcett, S. B. Majumder, G. E. J. Poinern, *Battery Energy* **2023**, *2*, 20230030.
[5] J. B. Goodenough, K.-S. Park, *J. Am. Chem. Soc.* **2013**, *135*, 1167.
[6] J. S. Newman, N. P. Balsara, *Electrochemical Systems*, Wiley, Hoboken, NJ **2019**.

[7] J.-G. Zhang, W. Xu, W. A. Henderson, *Lithium Metal Anodes and Rechargeable Lithium Metal Batteries*, Springer International Publishing, Cham **2017**, p. 1..

[8] D. Lin, Y. Liu, Y. Cui, *Nat. Nanotechnol.* **2017**, *12*, 194.

[9] X. Ji, L. F. Nazar, *J. Mater. Chem.* **2010**, *20*, 9821.

[10] G. Girishkumar, B. McCloskey, A. C. Luntz, S. Swanson, W. Wilcke, *J. Phys. Chem. Lett.* **2010**, *1*, 2193.

[11] C. Fang, X. Wang, Y. S. Meng, *Trends Chem.* **2019**, *1*, 152.

[12] F. Jiang, S. Yang, H. Liu, X. Cheng, L. Liu, R. Xiang, Q. Zhang, S. Kaskel, J. Huang, *SusMat* **2021**, *1*, 506.

[13] D.-H. Liu, Z. Bai, M. Li, A. Yu, D. Luo, W. Liu, L. Yang, J. Lu, K. Amine, Z. Chen, *Chem. Soc. Rev.* **2020**, *49*, 5407.

[14] M. V. Reddy, A. Mauger, C. M. Julien, A. Paolella, K. Zaghib, *Materials (Basel)* **2020**, *13*, 1884.

[15] M. Winter, B. Barnett, K. Xu, *Chem. Rev.* **2018**, *118*, 11433.

[16] M. S. Whittingham, *Chem. Rev.* **2004**, *104*, 4271.

[17] B. Horstmann, J. Shi, R. Amine, M. Werres, X. He, H. Jia, F. Hausen, I. Cekic-Laskovic, S. Wiemers-Meyer, J. Lopez, D. Galvez-Aranda, F. Baakes, D. Bresser, C.-C. Su, Y. Xu, W. Xu, P. Jakes, R.-A. Eichel, E. Figgemeier, U. Krewer, J. M. Seminario, P. B. Balbuena, C. Wang, S. Passerini, Y. Shao-Horn, M. Winter, K. Amine, R. Kostecki, A. Latz, *Energy Environ. Sci.* **2021**, *14*, 5289.

[18] G. Brunklaus, P. Lennartz, M. Winter, *Nat. Rev. Electr. Eng.* **2024**, *1*, 79.

[19] C. Jin, T. Liu, O. Sheng, M. Li, T. Liu, Y. Yuan, J. Nai, Z. Ju, W. Zhang, Y. Liu, Y. Wang, Z. Lin, J. Lu, X. Tao, *Nat. Energy* **2021**, *6*, 378.

[20] X. Gao, Y.-N. Zhou, D. Han, J. Zhou, D. Zhou, W. Tang, J. B. Goodenough, *Joule* **2020**, *4*, 1864.

[21] Y. Sun, T. Yang, H. Ji, J. Zhou, Z. Wang, T. Qian, C. Yan, *Adv. Energy Mater.* **2020**, *10*, 2002373.

[22] S. Yari, M. K. Van Bael, A. Hardy, M. Safari, *Batteries & Supercaps* **2022**, *5*, e202200217.

[23] Y. Gu, W. Wang, J. He, S. Tang, H. Xu, J. Yan, Q. Wu, X. Lian, M. Zheng, Q. Dong, B. Mao, *ChemElectroChem* **2019**, *6*, 181.

[24] X. Wang, M. Zhang, J. Alvarado, S. Wang, M. Sina, B. Lu, J. Bouwer, W. Xu, J. Xiao, J.-G. Zhang, J. Liu, Y. S. Meng, *Nano Lett.* **2017**, *17*, 7606.

[25] Z. Yu, P. E. Rudnicki, Z. Zhang, Z. Huang, H. Celik, S. T. Oyakhire, Y. Chen, X. Kong, S. C. Kim, X. Xiao, H. Wang, Y. Zheng, G. A. Kamat, M. S. Kim, S. F. Bent, J. Qin, Y. Cui, Z. Bao, *Nat. Energy* **2022**, *7*, 94.

[26] X. Yin, X. Li, X. Cui, L. Liu, X. Weng, S. Ding, W. Yu, *Batteries & Supercaps* **2023**, *6*, e202200394.

[27] B. G. Choobar, H. Modarress, R. Halladj, S. Amjad-Iranagh, *J. Phys. Chem. C* **2019**, *123*, 21913.

[28] H. Wang, Z. Yu, X. Kong, S. C. Kim, D. T. Boyle, J. Qin, Z. Bao, Y. Cui, *Joule* **2022**, *6*, 588.

[29] Z. Yu, H. Wang, X. Kong, W. Huang, Y. Tsao, D. G. Mackanic, K. Wang, X. Wang, W. Huang, S. Choudhury, Y. Zheng, C. V. Amanchukwu, S. T. Hung, Y. Ma, E. G. Lomeli, J. Qin, Y. Cui, Z. Bao, *Nat. Energy* **2020**, *5*, 526.

[30] X. Zhang, Q. J. Wang, K. L. Harrison, K. Jungjohann, B. L. Boyce, S. A. Roberts, P. M. Attia, S. J. Harris, *J. Electrochem. Soc.* **2019**, *166*, A3639.

[31] C. Fang, B. Lu, G. Pawar, M. Zhang, D. Cheng, S. Chen, M. Ceja, J.-M. Doux, H. Musrock, M. Cai, B. Liaw, Y. S. Meng, *Nat. Energy* **2021**, *6*, 987.

[32] G. Li, S. Xu, B. Li, M. Yin, F. Shao, H. Li, T. Xia, Z. Yang, Y. Su, Y. Zhang, J. Ma, J. Yu, N. Hu, *ChemElectroChem* **2021**, *8*, 3273.

[33] Z. Han, C. Zhang, Q. Lin, Y. Zhang, Y. Deng, J. Han, D. Wu, F. Kang, Q. Yang, W. Lv, *Small Methods* **2021**, *5*, 2001035.

[34] E. K. Jang, J. Ahn, S. Yoon, K. Y. Cho, *Adv. Funct. Mater.* **2019**, *29*, 1905078.

[35] E. Cha, H. Lee, W. Choi, *ChemElectroChem* **2020**, *7*, 890.

[36] J. Zheng, M. H. Engelhard, D. Mei, S. Jiao, B. J. Polzin, J.-G. Zhang, W. Xu, *Nat. Energy* **2017**, *2*, 17012.

[37] J. Wang, Y. Yamada, K. Sodeyama, C. H. Chiang, Y. Tateyama, A. Yamada, *Nat. Commun.* **2016**, *7*, 12032.

[38] X. Cao, H. Jia, W. Xu, J.-G. Zhang, *J. Electrochem. Soc.* **2021**, *168*, 010522.

[39] C. Brissot, M. Rosso, J.-N. Chazalviel, S. Lascaud, *J. Power Sources* **1999**, *81–82*, 925.

[40] M. Dollé, L. Sannier, B. Beaudoin, M. Trentin, J.-M. Tarascon, *Electrochem. Solid-State Lett.* **2002**, *5*, A286.

[41] M. S. Park, S. B. Ma, D. J. Lee, D. Im, S.-G. Doo, O. Yamamoto, *Sci. Rep.* **2014**, *4*, 3815.

[42] T. Foroozan, S. Sharifi-Asl, R. Shahbazian-Yassar, *J. Power Sources* **2020**, *461*, 228135.

[43] S. Wang, Q. Liu, C. Zhao, F. Lv, X. Qin, H. Du, F. Kang, B. Li, *Energy Environ. Mater.* **2018**, *1*, 28.

[44] Y. Liu, Z. Ju, B. Zhang, Y. Wang, J. Nai, T. Liu, X. Tao, *Acc. Chem. Res.* **2021**, *54*, 2088.

[45] S. Frisco, D. X. Liu, A. Kumar, J. F. Whitacre, C. T. Love, K. E. Swider-Lyons, S. Litster, *ACS Appl. Mater. Interfaces* **2017**, *9*, 18748.

[46] M. Kitta, H. Sano, *Langmuir* **2017**, *33*, 1861.

[47] Q. Li, H. Pan, W. Li, Y. Wang, J. Wang, J. Zheng, X. Yu, H. Li, L. Chen, *ACS Energy Lett.* **2018**, *3*, 2259.

[48] S. Wang, X. Yin, D. Liu, Y. Liu, X. Qin, W. Wang, R. Zhao, X. Zeng, B. Li, *J. Mater. Chem. A* **2020**, *8*, 18348.

[49] Q. Wang, C. Zhao, S. Wang, J. Wang, M. Liu, S. Ganapathy, X. Bai, B. Li, M. Wagemaker, *J. Am. Chem. Soc.* **2022**, *144*, 21961.

[50] D. Stępień, B. Wolff, T. Diemant, G.-T. Kim, F. Hausen, D. Bresser, S. Passerini, *ACS Appl. Mater. Interfaces* **2023**, *15*, 25462.

[51] H. Liu, Y. Ji, Y. Li, S. Zheng, Z. Dong, K. Yang, A. Cao, Y. Huang, Y. Wang, H. Shen, S. Zhang, F. Pan, L. Yang, *Interdiscip. Mater.* **2024**, *3*, 297.

[52] Z. Ju, J. Nai, Y. Wang, T. Liu, J. Zheng, H. Yuan, O. Sheng, C. Jin, W. Zhang, Z. Jin, H. Tian, Y. Liu, X. Tao, *Nat. Commun.* **2020**, *11*, 488.

[53] S.-H. Yu, X. Huang, J. D. Brock, H. D. Abruña, *J. Am. Chem. Soc.* **2019**, *141*, 8441.

[54] C. Fang, J. Li, M. Zhang, Y. Zhang, F. Yang, J. Z. Lee, M.-H. Lee, J. Alvarado, M. A. Schroeder, Y. Yang, B. Lu, N. Williams, M. Ceja, L. Yang, M. Cai, J. Gu, K. Xu, X. Wang, Y. S. Meng, *Nature* **2019**, *572*, 511.

[55] A. Papapetrou, *Z. Krist. - Cryst. Mater.* **1935**, *92*, 89.

[56] V. R. Howes, *Proc. Phys. Soc.* **1959**, *74*, 616.

[57] G. Wranglén, *Electrochim. Acta* **1960**, *2*, 130.

[58] J. Barton, J. O. Bockris, *Proc. R. Soc. London Ser. Math. Phys. Sci.* **1962**, *268*, 485.

[59] J.-N. Chazalviel, *Phys. Rev. A* **1990**, *42*, 7355.

[60] M. Rosso, T. Gobron, C. Brissot, J.-N. Chazalviel, S. Lascaud, *J. Power Sources* **2001**, *97–98*, 804.

[61] C. Monroe, J. Newman, *J. Electrochem. Soc.* **2004**, *151*, A880.

[62] C. Monroe, J. Newman, *J. Electrochem. Soc.* **2005**, *152*, A396.

[63] R. Akolkar, *J. Power Sources* **2013**, *232*, 23.

[64] C. Monroe, J. Newman, *J. Electrochem. Soc.* **2003**, *150*, A1377.

[65] X. Wang, W. Zeng, L. Hong, W. Xu, H. Yang, F. Wang, H. Duan, M. Tang, H. Jiang, *Nat. Energy* **2018**, *3*, 227.

[66] G. Liu, W. Lu, *J. Electrochem. Soc.* **2017**, *164*, A1826.

[67] H. Koshina, N. Eda, A. Morita, in *Ext. Abstr. 40th ISE Meet.*, Kyoto, Japan, September 17-22, **1989**, p. 520.

[68] J. Franks, *Acta Metall.* **1958**, *6*, 103.

[69] K. N. Tu, *Phys. Rev. B* **1994**, *49*, 2030.

[70] M. Arakawa, S. Tobishima, Y. Nemoto, M. Ichimura, J. Yamaki, *J. Power Sources* **1993**, *43*, 27.

[71] J. Yamaki, S. Tobishima, K. Hayashi, K. Saito, Y. Nemoto, M. Arakawa, *J. Power Sources* **1998**, *74*, 219.

[72] M. Dollé, L. Sannier, B. Beaudoin, M. Trentin, J.-M. Tarascon, *Electrochem. Solid-State Lett.* **2002**, *5*, A286.

[73] O. Crowther, A. C. West, *J. Electrochem. Soc.* **2008**, *155*, A806.

[74] P. Bai, J. Li, F. R. Brushett, M. Z. Bazant, *Energy Environ. Sci.* **2016**, *9*, 3221.

[75] A. Kushima, K. P. So, C. Su, P. Bai, N. Kuriyama, T. Maebashi, Y. Fujiwara, M. Z. Bazant, J. Li, *Nano Energy* **2017**, *32*, 271.

[76] A. Ferrese, P. Albertus, J. Christensen, J. Newman, *J. Electrochem. Soc.* **2012**, *159*, A1615.

[77] A. Ferrese, J. Newman, *J. Electrochem. Soc.* **2014**, *161*, A1350.

[78] A. Jana, S. I. Woo, K. S. N. Vikrant, R. E. García, *Energy Environ. Sci.* **2019**, *12*, 3595.

[79] A. Jana, R. E. García, *Nano Energy* **2017**, *41*, 552.

[80] D. R. Ely, R. E. García, *J. Electrochem. Soc.* **2013**, *160*, A662.

[81] J. Yamaki, S. Tobishima, K. Hayashi, K. Saito, Y. Nemoto, M. Arakawa, *J. Power Sources* **1998**, *74*, 219.

[82] R. Akolkar, *J. Power Sources* **2014**, *246*, 84.

[83] D. S. Sholl, J. A. Steckel, *Density Functional Theory: A Practical Introduction*, John Wiley & Sons, Hoboken, NJ, **2011**.

[84] D. Frenkel, B. Smit, *Understanding Molecular Simulation: From Algorithms to Applications*, Academic Press, San Diego, **2001**.

[85] Q. Wang, G. Zhang, Y. Li, Z. Hong, D. Wang, S. Shi, *Npj Comput. Mater.* **2020**, *6*, 176.

[86] M. Jäckle, K. Helmbrecht, M. Smits, D. Stottmeister, A. Groß, *Energy Environ. Sci.* **2018**, *11*, 3400.

[87] M. Jäckle, A. Groß, *J. Chem. Phys.* **2019**, *151*, 234707.

[88] I. Treu Røe, S. K. Schnell, *Mol. Phys.* **2022**, *120*, e2053217.

[89] M. Jäckle, A. Groß, *J. Chem. Phys.* **2014**, *141*, 174710.

[90] C. Ling, D. Banerjee, M. Matsui, *Electrochim. Acta* **2012**, *76*, 270.

[91] A. Hagopian, M.-L. Doublet, J.-S. Filhol, *Energy Environ. Sci.* **2020**, *13*, 5186.
[92] E. P. Kamphaus, K. Hight, M. Dermott, P. B. Balbuena, *Phys. Chem. Chem. Phys.* **2020**, *22*, 575.
[93] B. G. Choobar, H. Modarress, R. Halladj, S. Amjad-Iranagh, *Comput. Mater. Sci.* **2021**, *192*, 110343.
[94] A. Allagui, H. Benaoum, C. Wang, *J. Phys. Chem. C* **2022**, *126*, 3029.
[95] M. Z. Bazant, *Faraday Discuss.* **2023**, *246*, 60.
[96] D. T. Boyle, X. Kong, A. Pei, P. E. Rudnicki, F. Shi, W. Huang, Z. Bao, J. Qin, Y. Cui, *ACS Energy Lett.* **2020**, *5*, 701.
[97] B. G. Choobar, H. Hamed, M. Safari, *J. Energy Chem.* **2023**, *80*, 452.
[98] R. Kurchin, V. Viswanathan, *J. Chem. Phys.* **2020**, *153*, 134706.
[99] P. Bai, M. Z. Bazant, *Nat. Commun.* **2014**, *5*, 3585.
[100] E. Santos, W. Schmickler, *Angew. Chem. Int. Ed.* **2021**, *60*, 5876.
[101] F. Hao, A. Verma, P. P. Mukherjee, *ACS Appl. Mater. Interfaces* **2018**, *10*, 26320.
[102] Y. Liu, X. Xu, M. Sadd, O. O. Kapitanova, V. A. Krivchenko, J. Ban, J. Wang, X. Jiao, Z. Song, J. Song, S. Xiong, A. Matic, *Adv. Sci.* **2021**, *8*, 2003301.
[103] X. Xu, Y. Liu, J. Hwang, O. O. Kapitanova, Z. Song, Y. Sun, A. Matic, S. Xiong, *Adv. Energy Mater.* **2020**, *10*, 2002390.
[104] A. Aryanfar, A. Tayyar, W. A. Goddard, *Phys. Rev. E* **2023**, *108*, 014801.
[105] T. K. Schwietert, P. Ombrini, L. S. Ootes, L. Oostrum, V. Azizi, D. Cogswell, J. Zhu, M. Z. Bazant, M. Wagemaker, A. Vasileiadis, *PRX Energy* **2023**, *2*, 033014.
[106] Y. Liu, X. Xu, M. Sadd, O. O. Kapitanova, V. A. Krivchenko, J. Ban, J. Wang, X. Jiao, Z. Song, J. Song, S. Xiong, A. Matic, *Adv. Sci.* **2021**, *8*, 2003301.
[107] F. Hu, T. Song, *RSC Adv.* **2017**, *7*, 54203.
[108] M. C. H. Wolfram Koch, *A Chemist's Guide to Density Functional Theory*, Wiley-VCH, Weinheim, **2001**.
[109] L. E. Camacho-Forero, T. W. Smith, S. Bertolini, P. B. Balbuena, *J. Phys. Chem. C* **2015**, *119*, 26828.
[110] M. Gerasimov, F. A. Soto, J. Wagner, F. Baakes, N. Guo, F. Ospina-Acevedo, F. Röder, P. B. Balbuena, U. Krewer, *J. Phys. Chem. C* **2023**, *127*, 4872.
[111] C. F. N. Marchiori, R. P. Carvalho, M. Ebadi, D. Brandell, C. M. Araujo, *Chem. Mater.* **2020**, *32*, 7237.
[112] H. Haghkhah, B. G. Choobar, S. Amjad-Iranagh, *J. Mol. Model.* **2020**, *26*, 220.
[113] D. E. Galvez-Aranda, J. M. Seminario, *J. Phys. Chem. C* **2020**, *124*, 21919.
[114] P. Yu, Q. Sun, Y. Liu, B. Ma, H. Yang, M. Xie, T. Cheng, *ACS Appl. Mater. Interfaces* **2022**, *14*, 7972.
[115] M. Ebadi, C. Marchiori, J. Mindemark, D. Brandell, C. M. Araujo, *J. Mater. Chem. A* **2019**, *7*, 8394.
[116] M. Ebadi, L. T. Costa, C. M. Araujo, D. Brandell, *Electrochim. Acta* **2017**, *234*, 43.
[117] W. R. Tyson, *Can. Metall. Q.* **1975**, *14*, 307.
[118] M. J. Frisch, G. W. Trucks, H. B. Schlegel, Gaussian 16, Revision A.03, Gaussian, Inc., Wallingford CT,**2016**.
[119] M. Bin Jassar, C. Michel, S. Abada, T. De Bruin, S. Tant, C. Nieto-Draghi, S. N. Steinmann, *Adv. Funct. Mater.* **2024**, 34,2313188.
[120] V. Ponce, D. E. Galvez-Aranda, J. M. Seminario, *Phys. Chem. Chem. Phys.* **2021**, *23*, 597.
[121] S. Rezaee, H. Araghi, H. Noshad, Z. Zabihi, *Eur. Phys. J. Plus* **2022**, *137*, 1194.
[122] D. E. Galvez-Aranda, J. M. Seminario, *J. Electrochem. Soc.* **2021**, *168*, 090528.
[123] L. E. Camacho-Forero, T. W. Smith, P. B. Balbuena, *J. Phys. Chem. C* **2017**, *121*, 182.
[124] H. G. Lee, S. Y. Kim, J. S. Lee, *Npj Comput. Mater.* **2022**, *8*, 103.
[125] M. Zhou, C. Feng, R. Xiong, L. Li, T. Huang, M. Li, Y. Zhang, H. Zhou, *ACS Appl. Mater. Interfaces* **2022**, *14*, 24875.
[126] A. Pei, G. Zheng, F. Shi, Y. Li, Y. Cui, *Nano Lett.* **2017**, *17*, 1132.
[127] C. Wagner, *J. Electrochem. Soc.* **1951**, *98*, 116.
[128] C. Fang, A. Mistry, V. Srinivasan, N. P. Balsara, R. Wang, *JACS Au* **2023**, *3*, 306.
[129] F. Wohde, M. Balabajew, B. Roling, *J. Electrochem. Soc.* **2016**, *163*, A714.
[130] H. Arunachalam, S. Onori, I. Battiato, *J. Electrochem. Soc.* **2015**, *162*, A1940.
[131] I. S. S. Carrasco, S. G. Alves, F. D. A. Aarão Reis, *Phys. Chem. Chem. Phys.* **2022**, *24*, 27856.
[132] J. Jeon, G. H. Yoon, T. Vegge, J. H. Chang, *ACS Appl. Mater. Interfaces* **2022**, *14*, 15275.
[133] B. S. Vishnugopi, F. Hao, A. Verma, P. P. Mukherjee, *ACS Appl. Mater. Interfaces* **2020**, *12*, 23931.
[134] F. Ding, W. Xu, G. L. Graff, J. Zhang, M. L. Sushko, X. Chen, Y. Shao, M. H. Engelhard, Z. Nie, J. Xiao, X. Liu, P. V. Sushko, J. Liu, J.-G. Zhang, *J. Am. Chem. Soc.* **2013**, *135*, 4450.
[135] P. Hundekar, S. Basu, J. Pan, S. F. Bartolucci, S. Narayanan, Z. Yang, N. Koratkar, *Energy Storage Mater.* **2019**, *20*, 291.
[136] G. Yeo, J. Sung, M. Choi, N. Kim, M. Ko, *J. Mater. Chem. A* **2022**, *10*, 12938.
[137] C. Wang, A. Wang, L. Ren, X. Guan, D. Wang, A. Dong, C. Zhang, G. Li, J. Luo, *Adv. Funct. Mater.* **2019**, *29*, 1905940.
[138] X. Yang, Y. Wang, Y. Guo, Z. Y. Liao, W. Fu, J. Liu, *J. Mater. Chem. A* **2024**, DOI: 10.1039/D4TA01269K.
[139] J. Wang, W. Huang, A. Pei, Y. Li, F. Shi, X. Yu, Y. Cui, *Nat. Energy* **2019**, *4*, 664.
[140] H. Zhang, Y. Wang, J. Huang, W. Li, X. Zeng, A. Jia, H. Peng, X. Zhang, W. Yang, *Energy Environ. Mater.* **2024**, *7*, e12514.
[141] Q. Sun, Y. Xiang, Y. Liu, L. Xu, T. Leng, Y. Ye, A. Fortunelli, W. A. Goddard, T. Cheng, *J. Phys. Chem. Lett.* **2022**, *13*, 8047.
[142] T. Hu, J. Tian, F. Dai, X. Wang, R. Wen, S. Xu, *J. Am. Chem. Soc.* **2023**, *145*, 1327.
[143] A. Agrawal, S. Yari, H. Hamed, T. Gouveia, R. Lin, M. Safari, *Carbon Energy* **2023**, *5*, e355.
[144] K. M. Diederichsen, E. J. McShane, B. D. McCloskey, *ACS Energy Lett.* **2017**, *2*, 2563.
[145] Z. Samadi, S. Amjad-Iranagh, F. Rashidi, B. G. Choobar, H. Modarress, *Solid State Ionics* **2023**, *398*, 116256.
[146] M. Molashahi, H. Modarress, B. Nasernejad, S. Amjad-Iranagh, B. G. Choobar, *Macromolecules* **2022**, *55*, 10556.
[147] Y. Qiu, X. Zhang, Y. Tian, Z. Zhou, *Chin. J. Struct. Chem.* **2023**, *42*, 100118.
[148] X. Jiao, Y. Wang, O. O. Kapitanova, X. Xu, V. S. Volkov, Y. Liu, Z. Song, A. Matic, S. Xiong, *Energy Storage Mater.* **2023**, *61*, 102916.
[149] C. Zhao, T. Wada, V. De Andrade, D. Gürsoy, H. Kato, Y. K. Chen-Wiegart, *Nano Energy* **2018**, *52*, 381.
[150] A. Torayev, P. C. M. M. Magusin, C. P. Grey, C. Merlet, A. A. Franco, *ACS Appl. Energ. Mater.* **2018**, *1*, 6433.
[151] A. Etiemble, A. Tranchot, T. Douillard, H. Idrissi, E. Maire, L. Roué, *J. Electrochem. Soc.* **2016**, *163*, A1550.
[152] D. P. Finegan, I. Squires, A. Dahari, S. Kench, K. L. Jungjohann, S. J. Cooper, *ACS Energy Lett.* **2022**, *7*, 4368.
[153] T.-C. Chen, *Mater. Today Commun.* **2023**, *35*, 105858.
[154] V. Goel, K.-H. Chen, N. P. Dasgupta, K. Thornton, *Energy Storage Mater.* **2023**, *57*, 44.
[155] H. Xu, J. Zhu, D. P. Finegan, H. Zhao, X. Lu, W. Li, N. Hoffman, A. Bertei, P. Shearing, M. Z. Bazant, *Adv. Energy Mater.* **2021**, *11*, 2003908.
[156] H. Pan, T. Fu, G. Zan, R. Chen, C. Yao, Q. Li, P. Pianetta, K. Zhang, Y. Liu, X. Yu, H. Li, *Nano Lett.* **2021**, *21*, 5254.
[157] E. J. F. Dickinson, H. Ekström, E. Fontes, *Electrochem. Commun.* **2014**, *40*, 71.
[158] J. Steiger, D. Kramer, R. Mönig, *J. Power Sources* **2014**, *261*, 112.

Manuscript received: July 1, 2024
Revised manuscript received: August 20, 2024
Version of record online: October 23, 2024